Acta Materialia 199 (2020) 633–648

Contents lists available at ScienceDirect

Acta Materialia

journal homepage: www.elsevier.com/locate/actamat

Full length article

New inversion boundary structure in Sb-doped ZnO predicted by DFT calculations and confirmed by experimental HRTEM

Vesna Ribić[a,*], Aleksander Rečnik[b], Matej Komelj[b], Anton Kokalj[c], Zorica Branković[a], Mario Zlatović[d], Goran Branković[a]

[a] Institute for Multidisciplinary Research, University of Belgrade, Kneza Višeslava 1, Belgrade, Serbia
[b] Department for Nanostructured Materials, Jožef Stefan Institute, Jamova cesta 39, Ljubljana, Slovenia
[c] Department of Physical and Organic Chemistry, Jožef Stefan Institute, Jamova cesta 39, Ljubljana, Slovenia
[d] Department of Organic Chemistry, Faculty of Chemistry, University of Belgrade, Studentski trg 12-16, Belgrade, Serbia

ARTICLE INFO

Article history:
Received 14 May 2020
Revised 12 August 2020
Accepted 16 August 2020
Available online 20 August 2020

Keywords:
Inversion domain boundary (IDB)
Interfaces (twin boundaries, stacking faults)
Interface energy
Density functional theory (DFT)
Transmission electron microscopy (TEM)

ABSTRACT

Today, *ab-initio* calculations are becoming a powerful tool to perform virtual experiments that have the capacity to predict and to reproduce experimentally observed non-periodic features, such as interfaces, that are responsible for quantum properties of materials. In our paper we investigate 2D quantum-well structures, known as inversion boundaries (IB). Combining atomistic modeling, DFT calculations and HRTEM analysis we provide a new fundamental insight into the structure and stability of Sb-rich basal-plane IBs in ZnO. DFT screening for potential IB model was based on the known stacking deviations in originating wurtzite structure. The results show that the model with $A\beta-B\alpha-A\beta C-\gamma B-\beta C$ sequence (IB_3) is the most stable translation for Sb-doping, as opposed to previously accepted $A\beta-B\alpha-A\beta C-\gamma A-\alpha C$ (IB_2) model. The key to the stability of IB structures has been found to lie in their cationic stacking. We show that the energies of constituting stacking segments can be used to predict the stability of new IB structures without the need of further *ab-initio* calculations. DFT optimized models of IBs accurately predict the experimentally observed IB structures with lateral relaxations down to a precision of ~1 pm. The newly determined cation sublattice expansions for experimentally confirmed IB_2 and IB_3 models, $\Delta_{IB(Zn-Zn)}$ are +81 pm and +77 pm, whereas the corresponding O-sublattice contractions $\Delta_{IB(O-O)}$ are −53 pm and −57 pm, respectively. The refined structures will help to solve open questions related to their role in electron transport, phonon scattering, p-type conductivity, affinity of dopants to generate IBs and the underlying formation mechanisms, whereas the excellent match between the calculations and experiment demonstrated in our study opens new perspectives for prediction of such properties from first principles.

1. Introduction

Inversion boundaries in ZnO attract much attention as key structural element in electron transport [1,2], phonon scattering [2–4], and most likely, also the unexplained p-type conductivity [5,6]. All these effects are related to their quantum-well structure [4], arising from an abrupt polarity inversion across one-atomic-layer-wide chemically-induced planar defect [7,8]. Zinc oxide (ZnO) as a wide direct band gap (~3.4 eV), low cost, nontoxic semiconductor, finds wide-range of applications in electronics. Since Matsuoka reported nonlinear electrical characteristics of ZnO ceramics [9], ZnO became a subject of extensive research for its use in nonohmic resistors (varistors) for overvoltage protection of electrical devices [10]. Here, several metal oxides (*i.e.* Sb_2O_3, TiO_2) were shown to play a decisive role in grain growth and enhancement of nonlinear coefficient α [9]. Sb_2O_3 addition to ZnO has been primarily investigated for its role in electrical properties [1,10,11] and grain growth [7,12–14] in varistor ceramics, but most recently, the highlight shifted to its relation to the p-type conductivity [5,15,16], opening new prospectives in optoelectronics [5,15–19].

The connection between the addition of Sb_2O_3 and the formation of planar faults in ZnO was first observed by Trontelj and Kraševec [20] suggesting that they are Sb-rich stacking faults (SFs). Their structural identification was not a simple task,

---

[*] Corresponding author.
E-mail address: vesna.ribic@imsi.rs (V. Ribić).

https://doi.org/10.1016/j.actamat.2020.08.035
1359-6454/

demanding the efforts of several research groups over more than a decade. Employing high-resolution transmission electron microscopy (HRTEM) Kim and Goo [21] suggested that these faults are basal-plane inversion boundaries (b-IBs). Without evidence of the direction of inversion and disregarding the presence of Sb_2O_3 in their samples [22], they analyzed eight possible IB models. Based on quantitative HRTEM analysis they proposed head-to-head IB involving a basal-plane SF with oxygen at the interface. Although there are several shortcomings in their study due to the lack of experimental capabilities, their research was very significant, since they opened up a completely new direction of research that became essential to studies of the microstructure development and electrical properties of ZnO [7,12–14]. Based on previous work [20–23] and crystal-chemistry considerations, Senda and Bradt [24] deduced that these faults are Sb-rich inversion twins comprising a few (111) layers of $Zn_7Sb_2O_{12}$ spinel. Using dedicated scanning TEM (STEM) Bruley et al. [25] provided the first spectroscopic proof of antimony. Using spatial difference method, the authors showed that up to one monolayer of Sb is uniformly distributed on the IBs. Soon after, the first comprehensive study of Sb-rich IBs was published by McCoy et al. [26]. Based on TEM observations they reported that both IB configurations exist in Sb-doped ZnO ceramics, but finally proposed a head-to-head model with a random distribution of Sb and Zn in the IB plane. They also suggested that IBs form in the initial stages of sintering through segregation of Sb on ZnO surfaces. Their work had important implications for the IB formation mechanism [7].

Based on a polarity determination [27], accurate determination of IB chemistry [28] and quantitative HRTEM analysis with 3D model reconstruction from two projections, Rečnik and coworkers reported the complete atomic structure of Sb-rich IBs [8]. Two major conclusions were drawn from their work: (*i*) the average charge per octahedral site in the IB layer is 3+, and (*ii*) IBs adopt a head-to-head inversion and comprise a cubic close-packed (*ccp*) fault in the O-sublattice corresponding to a sphalerite-type SF. Following the 3+ charge rule, Sb^{5+} and Zn^{2+} are ordered in the 1:2 ratio, generating a periodic honeycomb arrangement within the IB plane, unrelated to *e.g.* kagome layers of $Zn_7Sb_2O_{12}$ spinel [23–26]. The in-plane ordering of Sb was later confirmed by high-angle annular dark-field scanning TEM (HAADF-STEM) [29–31]. Besides Sb^{5+}, the 3+ charge rule holds for all dopants that form head-to-head IBs, regardless of their oxidation state, *i.e.* In^{3+} [32–36], Fe^{3+} [37,38], Sn^{4+} [28,39,40], and Mn^{3+} [2]. In addition to the interface chemistry, Rečnik et al. [8] determined the translation state of IBs and suggested today's only-known model of Sb-doped b-IBs in ZnO. The reported stacking involves a single SF (SF_1), and differs from that of In-rich IB layers found in In_2O_3-ZnO homologous phases with two subsequent *ccp* SFs (SF_2) in the O-sublattice [32]. The In-type stacking was confirmed in all subsequent studies of In-rich IBs [36], as well as with other dopants, including Fe-rich IBs [37] and Sn-rich IBs [38]. However, just recently, Hoemke et al. reported a new stacking for Mn-rich IBs [2] in a pure wurtzite lattice, which makes this the third known type of IB translation.

With a wide range of dopants and diversity of translations, IBs represent an excellent model system for studying the formation mechanisms and the thermodynamic stability of growth defects in crystals. While there are many reports on *ab-initio* calculations of $ZnO\text{–}M_2^{x+}O_x$ homologous phases [32–36,38,39], there are only a few studies that would directly address the stability of IBs in ZnO. The first study of IBs, based on quantum chemical calculations, was published by Yankovich et al. [6] in the Sb-doped system, followed by Hoemke et al. on Mn-doped ZnO [2]. These studies were aimed at investigating the local structure and electronic properties of IBs. From the thermodynamic point of view, it is interesting that three unique translations were experimentally determined for IBs in ZnO [2,8,34] and the question arises as to which of these translations is the most stable one, and whether different translations are possible for a particular dopant. Recently, Li et al. [41] compared the stability of dopant-free IBs by means of first-principle calculations, using the Kim and Goo models [21], whereas to date, no comparative study has been made for doped systems.

Here, Sb-rich IBs were used as a model system to study the stability of basal-plane IBs in ZnO. All three reported translations with additional, hypothetically possible IB models were analyzed by means of first-principles calculations. To support the calculations, IBs in Sb_2O_3-doped ZnO ceramics were reexamined using quantitative HRTEM analysis with image simulations of relaxed IB models.

2. Crystallography of IBs

2.1. ZnO structure

To understand the structural operations involved in IBs, let us first take a look at the ZnO structure. It crystallizes in the wurtzite structure modification [42], belonging to the $P6_3mc$ space group, with unit-cell parameters: $a = 3.2501$ Å, $c = 5.2071$ Å, and $u = 0.3817$ [43]. The structure is composed of close-packed planes of O and Zn, alternating in a hexagonal stacking (*hcp*) along the *c*-axis. In the wurtzite structure there are two types of tetrahedral interstices, type-I and type-II that point in opposite directions along the *c*-axis, and the octahedral interstices in-between. Zinc atoms occupy only one type of the tetrahedral sites, resulting in the noncentrosymmetric character of this structure along the crystallographic *c*-axis, with a polar vector pointing from the Zn to the O atom above it (Fig. 1), whereas the parameter u is defined as the distance between these two atoms in fractional units. If we use Greek letters (α,β,γ) to represent the Zn, and the Latin (A,B,C) for the O atoms, the *hcp* stacking of the wurtzite structure can be presented using the following expressions:

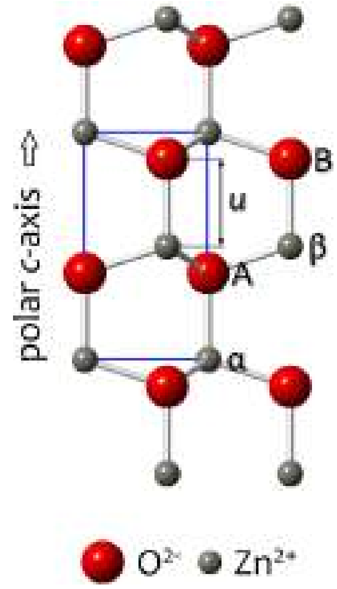

Fig. 1. ZnO wurtzite structure in $[2\bar{1}\bar{1}0]$ projection with indicated tetrahedral type-I (Zn^{2+}), tetrahedral type-II (empty) and octahedral (empty) sites. The unit cell is outlined in blue. (For interpretation of the references to color in this figure legend, the reader is referred to the web version of this article.)

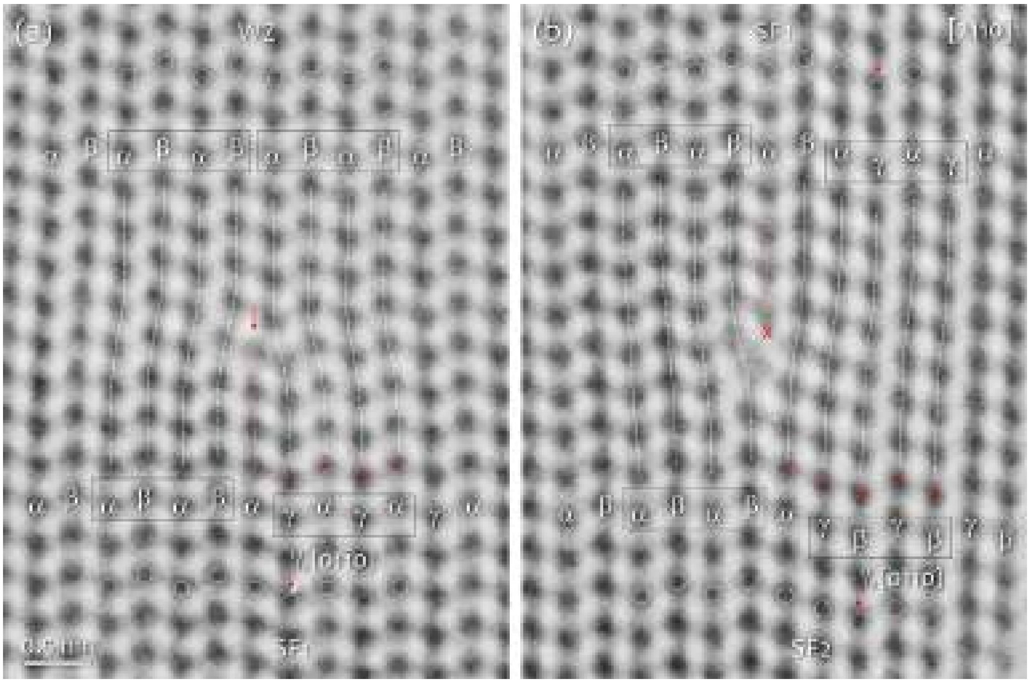

Fig. 2. HRTEM images of the two most common SFs in ZnO: (**a**) SF_1 forming in perfect ZnO lattice by the insertion (↓) of one close-packed Zn–O plane (indicated by red arrow). Following this operation the $B\alpha-A\beta-B\alpha-A\beta$ sequence glides into the $A\gamma-C\alpha-A\gamma-C\alpha$ sequence (see Eq. (4–2)). (**b**) SF_2 forming from SF_1 by termination (×) of the adjacent cp plane whereby the $A\gamma-C\alpha-A\gamma-C\alpha$ sequence further glides into $B\gamma-C\beta-B\gamma-C\beta$ (Eq. (5–2)). (For interpretation of the references to color in this figure legend, the reader is referred to the web version of this article.)

$$\ldots A\beta - B\alpha \ldots \tag{1}$$

Cubic close-packed (*ccp*) analogue of the wurtzite structure is sphalerite:

$$\ldots A\beta - B\gamma - C\alpha \ldots \tag{2}$$

a metastable polymorph of ZnO [44] found in confined geometries [45]. Owing to close structural relation, sphalerite-type SFs are common in ZnO [46].

2.2. Stacking faults

A stacking fault in a hexagonal close-packed lattice is accomplished by the removal (or insertion) of one close-packed (*cp*) plane, which must be followed by a $\vec{\mathbf{r}}_{SF} = \pm ⅓ [01\bar{1}0]$ glide to retain the regular stacking of the layers. Crystallographically, both operations lead to the same result (*see* Fig. S1), but what actually happens can be seen in the real lattices. The experimental evidence for the two most common types of SFs (SF_1 and SF_2) in ZnO are shown in the HRTEM images of Fig. 2. It can be seen that SF_1 is produced by the insertion of an extra *cp* plane (*e.g.* $B\alpha$) into the $A\beta-B\alpha$ wurtzite sequence (Fig. 2a). SF_2, on the other hand, seems to be linked to the preexisting SF_1, followed by removal of the adjacent *cp* plane, introducing another $\vec{\mathbf{r}}_{SF}$ glide (Fig. 2b). SF_2 apparently does not form directly from the ZnO lattice by a full ⅔ $[01\bar{1}0]$ glide, but necessitates the presence of SF_1. The strain produced by the $\vec{\mathbf{r}}_{SF}$ glide is compensated locally around an edge dislocation that introduces (labeled by ↓) or terminates (labeled by ×) the extra *cp* plane. Based on this observation, the formation of SF_1 is extrinsic, whereas the formation of SF_2 is intrinsic. More complex *hcp-ccp* sequences are possible, as reported by Yan et al. [46].

2.3. Inversion boundaries

In non-centrosymmetric crystals, an IB is defined as a plane, where the polarity is reversed. Domains of inverted polarity were discovered by etching of ZnO [47,48]. Today it is known that IBs in ZnO are formed by the addition of specific dopants with oxidation states higher than Zn^{2+}, these include: In^{3+} [32–36], Fe^{3+} [37,38], Mn^{3+} [2], Ga^{3+} [4,49], Si^{4+} [50], Sn^{4+} [39,40,51], Ti^{4+} [52,53] and Sb^{5+} [6,8,26,30]. Depending on the type of inversion the polar c-axis can be either head-to-head (→|←) or tail-to-tail (←|→) oriented across the IB plane. They principally lie in the basal planes (b-IB); nevertheless, some dopants, such as Ga^{3+} [49], produce inversion twins (IT), running along the pyramidal planes (p-IB) of the ZnO structure. The most common type of IBs are head-to-head b-IBs, characterized by the basal-plane octahedral layer with an in-plane dopant distribution following the 3+ charge rule [8]. If we carefully examine the reported stacking sequences it is evident that apart from the wurtzite structure [2], IBs can comprise different *ccp* sequences that are inherent to the sphalerite-type SFs [8,37]. Following the translations, based on atomic-scale TEM studies, we can construct three types of IBs that differ in the stacking of the O-sublattice. In addition to these, we include two additional low-energy O-sublattice violations [46].

Let us construct a b-IB in non-faulted ZnO lattice (Eqs. (3–1) to 3–3). This most simple model does not include SFs but only the inversion of polarity. Head-to-head inversion is accomplished by shifting the Zn^{2+} atoms from type-I to type-II face-sharing tetrahedral sites in the right half (R-domain) after the selected Zn-plane (α or β) that is to become an IB. While in the left half (L-domain) the Zn positions remain unchanged, the translation of Zn atoms (I) in the R-domain into their counter sites (II) equals to the $\vec{\mathbf{r}}_{IB} = -(1\text{-}2u)[0002]$. Hence, the total translation of IB_1 can be written as:

$$[\ldots A\beta_I\text{–}B\alpha_I\text{–}A\beta_I\text{–}B\alpha_I\text{–}A]_L\text{–}[\beta_I]_{IB}\text{–}[B\overset{\curvearrowleft}{\alpha_I}\text{–}A\overset{\curvearrowleft}{\beta_I}\text{–}B\overset{\curvearrowleft}{\alpha_I}\text{–}A\overset{\curvearrowleft}{\beta_I}\ \ldots]_R * \vec{\mathbf{r}}_{IB} \tag{3–1}$$

$$[\ldots A\beta_I\text{–}B\alpha_I\text{–}A\beta_I\text{–}B\alpha_I\text{–}A]_L\text{–}[\beta_I,\alpha_{II}]_{IB}\text{–}[B\text{–}\beta_{II}A\text{–}\alpha_{II}B\text{–}\beta_{II}A\ \ldots]_R \qquad \text{inversion} \tag{3–2}$$

$$[\ldots A\beta_I\text{–}B\alpha_I\text{–}A\beta_I\text{–}B\alpha_I\text{–}A]_L\text{–}[\ \gamma_{oct}\ ]_{IB}\text{–}[B\text{–}\beta_{II}A\text{–}\alpha_{II}B\text{–}\beta_{II}A\ \ldots]_R \qquad \text{IB}_1 \tag{3–3}$$

where Eq. (3–1) shows the wurtzite stacking divided into the L-domain, IB-plane and R-domain of which the Zn atoms are to be translated by the $\vec{\mathbf{r}}_{IB}$ from type-I tetrahedra to its symmetry-related type-II counterpart. In Eq. (3–2) the Zn-II atoms (blue letters indicate changing positions, red Greek letters indicate cation layers that become an IB-plane) jump to their counterpart type-II tetrahedral sites ($\alpha_I \rightarrow \alpha_{II}$, $\beta_I \rightarrow \beta_{II}$) by crossing the adjacent O-plane (B or A), and finally, in Eq. (3–3), the IB-plane Zn atoms occupying both tetrahedral sites (β_I, α_{II}) are replaced by octahedral interstitials (γ_{oct}). Here, only the Zn atoms in the R-domain are translated, whereas the O-sublattice remains unchanged, as in wurtzite. This IB-model (IB_1) was reported for Mn-doped ZnO by Hoemke et al. [2], and is not known for any other dopant.

The second IB model involves a sphalerite-type stacking fault (SF_1); *i.e.* a local *ccp* disruption in a *hcp* O-sublattice. Crystallographically, the translational state of SF_1 is described by 180° rotation of the R-domain around the (0001)-plane normal to any O-site. SF_1 is alternatively produced by the addition (or removal) of a $B\alpha_I$ (or $A\beta_I$) ZnO layer, followed by the $\vec{\mathbf{r}}_{SF} = \pm ⅓\ [01\bar{1}0]$ glide of the R-domain giving rise to local *ccp* stacking (Fig. 2a). The $\vec{\mathbf{r}}_{SF}$ has a positive sign if the added layer is $B\alpha_I$, and a negative, if the layer is $A\beta_I$, and vice-versa, if the layer is removed. All extrinsic and intrinsic modes are shown in the Supplementary material, Fig. S1. Using these operations, the translations involved in IB_2 can be written as:

$$[\ldots A\beta_I\text{–}B\alpha_I\text{–}A\beta_I\text{–}B\alpha_I]_L\text{–}[\overset{B\alpha_I\downarrow}{\square}\text{–}A\beta_I\text{–}B\alpha_I\text{–}A\beta_I\text{–}B\alpha_I\ \ldots]_R * \vec{\mathbf{r}}_{SF} \qquad \text{extrinsic} \tag{4–1}$$

$$[\ldots A\beta_I\text{–}B\alpha_I\text{–}A\beta_I\text{–}B\alpha_I]_L\text{–}[A\gamma_I\text{–}C\alpha_I\text{–}A\gamma_I\text{–}C\alpha_I\text{–}A\gamma_I\ \ldots]_R \qquad \text{SF}_1 \tag{4–2}$$

$$[\ldots A\beta_I\text{–}B\alpha_I\text{–}A\beta_I\text{–}B\alpha_I\text{–}A]_L\text{–}[\gamma_I]_{IB}\text{–}[C\alpha_I\text{–}A\gamma_I\text{–}C\alpha_I\text{–}A\gamma_I\ \ldots]_R * \vec{\mathbf{r}}_{IB} \qquad \text{inversion} \tag{4–3}$$

$$[\ldots A\beta_I\text{–}B\alpha_I\text{–}A\beta_I\text{–}B\alpha_I\text{–}A]_L\text{–}[\gamma_I,\alpha_{II}]_{IB}\text{–}[C\text{–}\gamma_{II}A\text{–}\alpha_{II}C\text{–}\gamma_{II}A\ \ldots]_R \tag{4–4}$$

$$[\ldots A\beta_I\text{–}B\alpha_I\text{–}A\beta_I\text{–}B\alpha_I\text{–}A]_L\text{–}[\ \beta_{oct}\ ]_{IB}\text{–}[C\text{–}\gamma_{II}A\text{–}\alpha_{II}C\text{–}\gamma_{II}A\ \ldots]_R \qquad \text{IB}_2 \tag{4–5}$$

where Eq. (4–1) shows the wurtzite stacking with an insertion of the $B\alpha_I$ layer. As two identical layers can not coexist, the complete R-domain along with the inserted layer is shifted so that $B\alpha_I \rightarrow A\gamma_I$ and $A\beta_I \rightarrow C\alpha_I$ to produce SF_1 (Eq. (4–2)). This is followed by inversion of the type-I tetrahedral sites into type-II sites in the R-domain except for the added $B\alpha_I \rightarrow A\gamma_I$ plane that becomes an IB (Eq. (4–3)). The doubly occupied tetrahedral sites (γ_I, α_{II}) in the IB layer (Eq. (4–4)) are replaced by octahedral (β_{oct}) sites (Eq. (4–5)). The complete operation of IB_2 is a 2-fold rotoinversion ($\bar{2}$) along [0002] at any vertex in the O-sublattice. This type of IBs including the local *ccp* stacking in O-sublattice that corresponds to SF_1 was proposed by Rečnik et al. [8] and confirmed in other studies of Sb-doped ZnO.

The third, most frequently reported model for IBs involves another type of stacking fault, *i.e.*, SF_2. It has a slightly higher energy than SF_1 [46] and is less common. SF_2 is produced by two 2-fold rotations in two successive (0002) planes, as described for SF_1, or, alternatively, by adding two consecutive $B\alpha_I$ (or $A\beta_I$) layers of the same type in a similar manner as in SF_1:

$$[\ldots A\beta_I\text{–}B\alpha_I\text{–}A\beta_I\text{–}B\alpha_I]_L\text{–}[\overset{B\alpha_I\downarrow}{\square}\text{–}[\overset{\times 2\downarrow}{\square}\text{–}A\beta_I\text{–}B\alpha_I\text{–}A\beta_I\text{–}B\alpha_I\ \ldots]]_R * \vec{\mathbf{r}}_{SF} \qquad \text{extrinsic} \times 2 \tag{5–1}$$

$$[\ldots A\beta_I\text{–}B\alpha_I\text{–}A\beta_I\text{–}B\alpha_I]_L\text{–}[A\gamma_I\text{–}[C\beta_I\text{–}B\gamma_I\text{–}C\beta_I\text{–}B\gamma_I\text{–}C\beta_I\ \ldots]]_R \qquad \text{SF}_2 \tag{5–2}$$

$$[\ldots A\beta_I\text{–}B\alpha_I\text{–}A\beta_I\text{–}B\alpha_I\text{–}A]_L\text{–}[\gamma_I]_{IB}\text{–}[C\beta_I\text{–}B\gamma_I\text{–}C\beta_I\text{–}B\gamma_I\ \ldots]_R * \vec{\mathbf{r}}_{IB} \qquad \text{inversion} \tag{5–3}$$

$$[\ldots A\beta_I\text{–}B\alpha_I\text{–}A\beta_I\text{–}B\alpha_I\text{–}A]_L\text{–}[\gamma_I,\alpha_{II}]_{IB}\text{–}[C\text{–}\gamma_{II}B\text{–}\beta_{II}C\text{–}\gamma_{II}B\ \ldots]_R \tag{5–4}$$

$$[\ldots A\beta_I\text{–}B\alpha_I\text{–}A\beta_I\text{–}B\alpha_I\text{–}A]_L\text{–}[\ \beta_{oct}\ ]_{IB}\text{–}[C\text{–}\gamma_{II}B\text{–}\alpha_{II}C\text{–}\gamma_{II}B\ \ldots]_R \qquad \text{IB}_3 \tag{5–5}$$

Here, following the rules described above, two layers of the same type are consecutively inserted and shifted by the $\vec{\mathbf{r}}_{SF}$ along with the R-domain (Eq. (5–1)) to produce two successive *ccp* layers (Fig. 2b). Brackets indicate sequentially shifted blocks, *i.e.* after outer, the inner undergoes the same shift to generate SF_2 (Eq. (5–2)). It could also be produced by the additional $\vec{\mathbf{r}}_{SF}$-shift from SF_1. This is followed by inversion (Eq. (5–3)) to the point of the highest symmetry at the mid of the *ccp* stacking (Eq. (5–4)). To achieve this, (β_I)-Zn atoms across the IB-plane must cross a *ccp* violation of the regular *hcp* stacking, following the inversion vector of $\vec{\mathbf{r}}_{ZB} = \vec{\mathbf{r}}_{IB} + 2\vec{\mathbf{r}}_{SF}$ for this layer resulting in $\beta_I \rightarrow \alpha_{II}$ (instead of β_{II}) in the IB plane. Tetrahedral (γ_I, α_{II}) sites are replaced by central octahedral (β_{oct}) sites to form IB_3 (Eq. (5–5)). This type of IB was first determined in the ZnO–In_2O_3 homologous phases [32–36], and subsequently also in Fe- [37] and Sn-rich IBs [40]. Given the fact that SF_2 are less stable than SF_1 or the fault-free ZnO structure [46] it is interesting that IB_3 are far more frequent than IB_2 or IB_1.

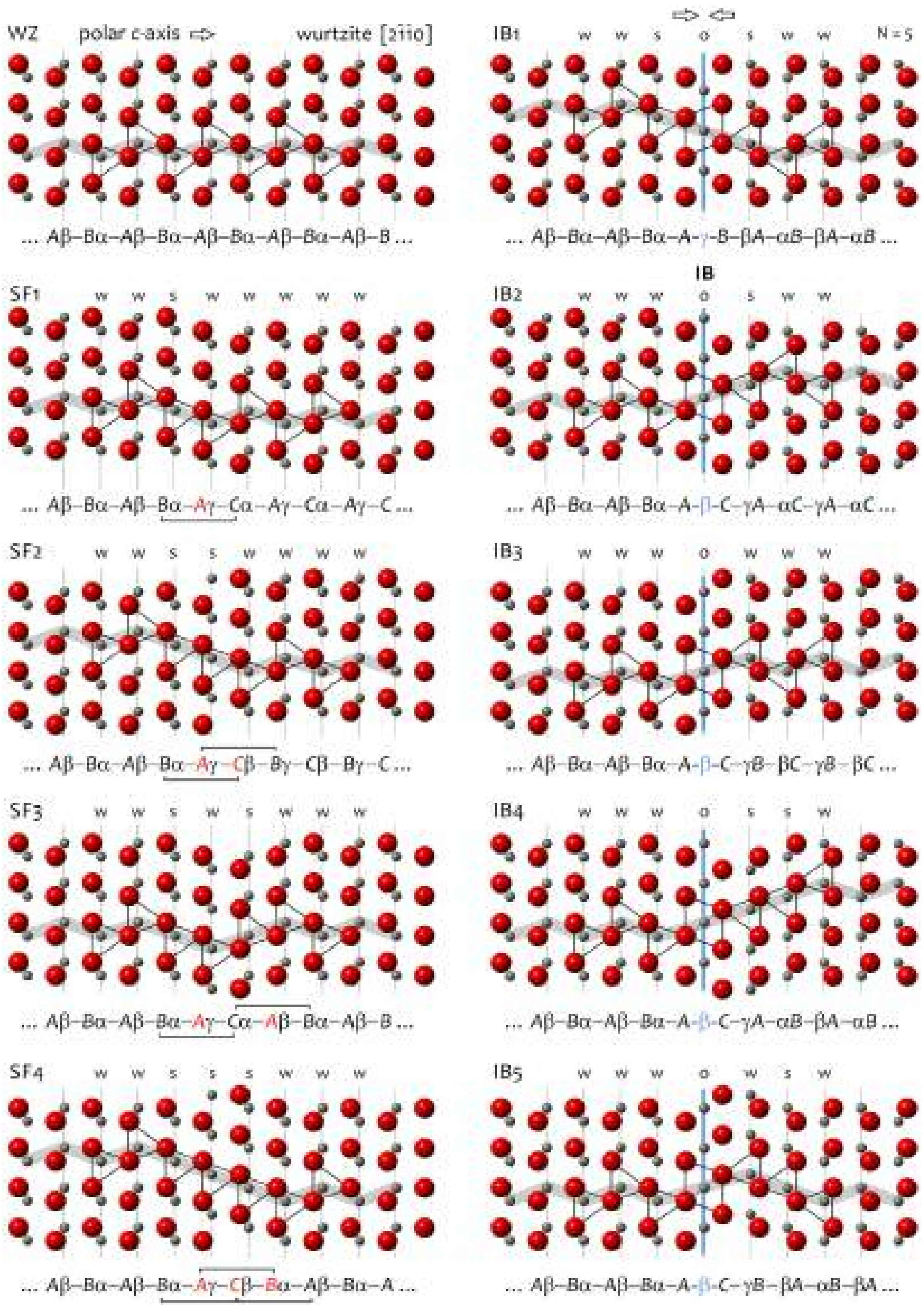

Fig. 3. Originating wurtzite/SF (*left*) and the resulting IB structures (*right*) with corresponding stacking sequences viewed in the $[2\bar{1}\bar{1}0]$ projection. Stacking violations in the SF_1–SF_4 models in the O-sublattice are highlighted by a red Latin letter and the *ccp* sequence is indicated by a horizontal bracket. Outlined tetrahedral and octahedral sites (*black*) indicate occupied interstices. Note the reversal of the occupied tetrahedral sites in IB models across the octahedral plane (highlighted by a *blue* vertical line and a Greek letter in the sequence). Cation sites are marked with the *black* dotted vertical lines and their stacking with Latin letters: w, s and o; sequence highlighted *grey*. (For interpretation of the references to color in this figure legend, the reader is referred to the web version of this article.)

Two further types of SFs are reported in the wurtzite structure [46]. They are characterized by an even higher complexity of stacking and have not yet been experimentally observed in ZnO.

The first one is obtained by a 180° rotation of a wurtzite ($A\beta-B\alpha$) slab around the normal of the (0002)-plane. Alternatively, the same stacking is obtained by the insertion of the wurtzite slab in a sequence that duplicates the adjacent layers, followed by the $\vec{\mathbf{r}}_{SF}$ shift; *i.e.* if the last layer is $A\beta$, the slab starts with $A\beta$, and vice-versa. SF_3 is followed by an inversion to the symmetry midpoint:

$$[\ldots A\beta_I-B\alpha_I-A\beta_I-B\alpha_I]_L-[\overset{B\alpha_I-A\beta_I\downarrow}{\square}-A\beta_I-B\alpha_I-A\beta_I-B\alpha_I\ \ldots]_R*\vec{\mathbf{r}}_{SF} \qquad \text{extrinsic } hcp \tag{6–1}$$

$$[\ldots A\beta_I-B\alpha_I-A\beta_I-B\alpha_I]_L-[A\gamma_I-C\alpha_I-A\beta_I-B\alpha_I-A\beta_I-B\alpha_I\ \ldots]_R \qquad SF_3 \tag{6–2}$$

$$[\ldots A\beta_I-B\alpha_I-A\beta_I-B\alpha_I-A]_L-[\gamma_I]-[C\alpha_I-A\beta_I-B\alpha_I-A\beta_I-B\alpha_I\ \ldots]_R*\vec{\mathbf{r}}_{IB} \qquad \text{inversion} \tag{6–3}$$

$$[\ldots A\beta_I-B\alpha_I-A\beta_I-B\alpha_I-A]_L-[\gamma_I,\alpha_{II}]-[C-\gamma_{II}A-\alpha_{II}B-\beta_{II}A-\alpha_{II}B\ \ldots]_R \tag{6–4}$$

$$[\ldots A\beta_I-B\alpha_I-A\beta_I-B\alpha_I-A]_L-[\ \beta_{oct}\ ]-[C-\gamma_{II}A-\alpha_{II}B-\beta_{II}A-\alpha_{II}B\ \ldots]_R \qquad IB_4 \tag{6–5}$$

where the full wurtzite slab is inserted and shifted within the wurtzite lattice (Eq. (6–1)) to produce SF_3 (6–2). This is followed by the inversion of the R-domain to the half of the inserted layer (6–3), which involves a $\beta_I \rightarrow \gamma_{II}$ (instead of β_{II}) transition over the *ccp* disruption that was produced symmetrically within the R-domain (Eq. (6–4)), similar to that in IB_3. Finally, the tetrahedral (γ_I, α_{II}) sites are replaced by the central octahedral (β_{oct}) sites to form IB_4 (Eq. (6–5)). This type of IB has not yet been confirmed experimentally.

The last of the stacking variants that we must take into account when considering b-IB models is the violation of wurtzite stacking with a full sphalerite slab [46], *i.e.* an $\vec{\mathbf{r}}_{ZB}$ translation. Similar to SF_3, the slab begins with the same sequence as the last layer of the wurtzite lattice at the insertion point. This is followed by the full $\vec{\mathbf{r}}_{ZB}$ shift of the slab. Like in SF_3, the host undergoes no translation:

$$[\ldots A\beta_I-B\alpha_I-A\beta_I-B\alpha_I]_L-[\overset{A\gamma_I-C\beta_I-B\alpha_I\downarrow}{\square}-A\beta_I-B\alpha_I-A\beta_I\ \ldots]_R*\vec{\mathbf{r}}_{ZB} \qquad \text{extrinsic } ccp \tag{7–1}$$

$$[\ldots A\beta_I-B\alpha_I-A\beta_I-B\alpha_I]_L-[A\gamma_I-C\beta_I-B\alpha_I-A\beta_I-B\alpha_I-A\beta_I\ \ldots]_R \qquad SF_4 \tag{7–2}$$

$$[\ldots A\beta_I-B\alpha_I-A\beta_I-B\alpha_I-A]_L-[\gamma_I]-[C\beta_I-B\alpha_I-A\beta_I-B\alpha_I-A\beta_I\ \ldots]_R*\vec{\mathbf{r}}_{IB} \qquad \text{inversion} \tag{7–3}$$

$$[\ldots A\beta_I-B\alpha_I-A\beta_I-B\alpha_I-A]_L-[\gamma_I,\alpha_{II}]-[C-\gamma_{II}B-\beta_{II}A-\alpha_{II}B-\beta_{II}A\ \ldots]_R \tag{7–4}$$

$$[\ldots A\beta_I-B\alpha_I-A\beta_I-B\alpha_I-A]_L-[\ \beta_{oct}\ ]-[C-\gamma_{II}B-\beta_{II}A-\alpha_{II}B-\beta_{II}A\ \ldots]_R \qquad IB_5 \tag{7–5}$$

with a full sphalerite ($A\gamma_I-C\beta_I-B\alpha_I$) slab inserted between the $B\alpha_I-A\beta_I$ wurtzite sequence (Eq. (7–1)), by which the wurtzite stacking in the SF_4 remains undisturbed (Eq. (7–2)). Upon the inversion of the R-domain, Zn atoms from the tetrahedral type-I sites are translated to type-II sites until the symmetric mid point. In this way, the inversion operation traverses two *ccp* sequences (Eq. (7–3)); A-B-C and B-C-A in reverse order), where the polarity reversal follows the *ccp* rule: $\alpha_I \rightarrow \gamma_{II}$ (instead of α_{II}), and $\beta_I \rightarrow \alpha_{II}$ (instead of β_{II}), respectively (Eq. (7–4)). Finally, the complete stacking of IB_5 is accomplished by replacement of two tetrahedral (γ_I, α_{II}) interstices with central octahedral (β_{oct}) sites. Similar to IB_4, also this type of inversion has also not yet been reported experimentally.

The SF and IB models with the corresponding stacking sequences are illustrated in Fig. 3. It can be seen that while O-sublattices remain unchanged in the IB models, cation sublattices undergo significant changes. For example, in IB_1 model, where the originating stacking of O and Zn atoms follows the wurtzite sequence, the O-stacking remains unchanged upon inversion (BABAB), but the Zn-stacking endures the transition to three consecutive *ccp* sequences: $\beta_I\alpha_I\gamma_{oct}-\alpha_I\gamma_{oct}\beta_{II}-\gamma_{oct}\beta_{II}\alpha_{II}$ (Eq. (3–3)). In a similar manner, the cationic sequences are crucially modified in other IB models. Thus, the symmetry implied by the O-sublattice does not anymore hold in the cation sublattice. As the regular stacking notation does not give a direct insight into the stacking violations we will use a simplified notation that takes into account the first neighbors. Hence, cations that reside in *hcp* surroundings (regular wurtzite structure) can be denoted as wurtzite tetrahedral (*w*), cations in *ccp* surroundings (*e.g.* SF) as sphalerite tetrahedral (*s*), and the cations in the IB plane, as octahedral (*o*). Using this notation, the cation sublattice in ZnO is written as ..*wwwww*.., SF_1 as ..*wswww*.., IB_1 as ..*wsosw*.., *etc*. (*see* Fig. 3).

3. Experimental methods

To investigate which of the proposed IB (1–5) models is thermodynamically the most stable we employed *ab-initio* calculations, followed by an experimental HRTEM study of the IBs in Sb_2O_3-doped ZnO ceramics to verify the validity of the DFT predictions.

3.1. Computational method

Ab-initio calculations were performed in the framework of the DFT using the generalized gradient approximation (GGA) of Perdew-Burke-Ernzerhof (PBE) [54] as implemented in the Quantum ESPRESSO package [55]. The valence electrons were described with a plane-wave basis set using the energy cutoff of 30 Ry (240 Ry for charge-density cutoff), whereas the core electrons were treated implicitly with ultra-soft pseudopotentials [56,57] (for Zn the 3d electrons were included in the valence shell). Brillouin zone integrations were performed with the uniform 4 × 4 × 4 k-mesh for ZnO bulk, the gamma point for the supercells (*see* Section 3.2), and the Marzari-Vanderbilt cold smearing of 0.02 Ry. The convergence threshold for self-consistency was 10^{-6} Ry. Before constructing the supercells, DFT optimization of the wurtzite-type and

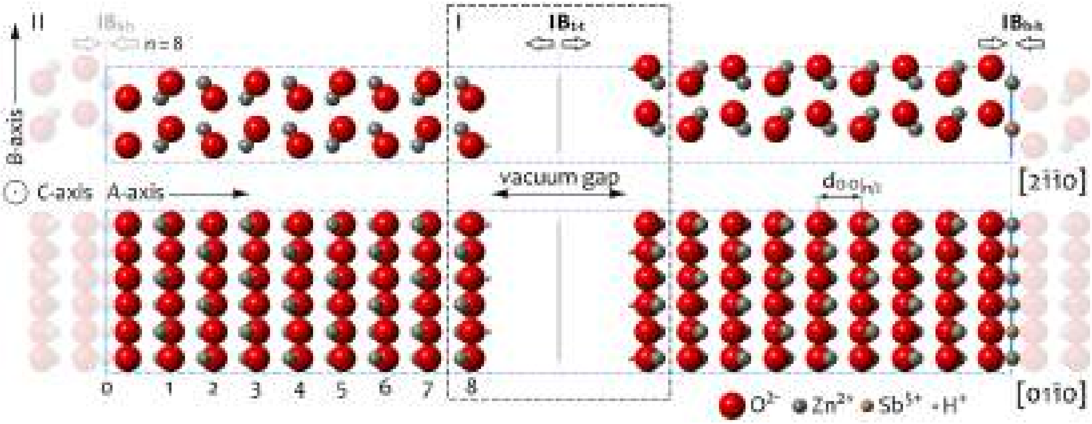

Fig. 4. Multi-slab design of supercells for DFT calculations. In this geometry, the *C* and *B*-axes are periodic, while the thickness of the slab along the *A*-axis is finite (n) to accommodate the discontinuity due to the polarity inversion. The IB-plane is composed of Sb and Zn atoms in a 1:2 honeycomb arrangement [8]. A sufficient number of Zn-O layers ($n = 8$) is added on each side of the IB-plane following the translation rules. To minimize tail-to-tail interactions, the slabs are separated by an 8 Å thick vacuum layer (*gap*) between the last and the first O-layer of the supercell. To satisfy the stoichiometry of the supercell, O-terminated surfaces of the slab are saturated by H atoms (*i.e.* 50% of the dangling O-ions are saturated, forming -OH groups). The illustrated multi-slab design of the IB employs the translation state of the IB$_2$ (Eq. (4–5)), shown in two low-index crystallographic projections of ZnO.

sphalerite-type ZnO were performed. The resulting unit-cell parameters of the wurtzite ZnO are: $a = 3.276$ Å, $c = 5.288$ Å, and $u = 0.379$, whereas unit-cell parameter of the sphalerite ZnO is: $a = 4.629$ Å. These values are in agreement with other theoretical studies [42,58].

3.2. Construction of the supercells

Following crystallographic operations described in the previous section, all five IB models were constructed in an orthorhombic geometry using the CrystalMaker® software [59]. In these supercells, the *A*-axis is chosen parallel to the [0001]-axis, the *B*-axis parallel to [01$\bar{1}$0], and the *C*-axis parallel to [2$\bar{1}\bar{1}$0] axis of the ZnO structure, respectively. To satisfy the reported in-plane distribution of the Sb and Zn atoms (in the 1:2 ratio) [8], the length of the *B*-axis must be multiplied by a factor of three. With this condition, the *B*- and *C*-directions become periodic, whereas the *A*-axis possesses no periodicity due to the presence of an IB. The IB-plane is placed at the mid of the *A*-dimension, followed by an identical number of Zn–O layers (n) from both sides, which finally defines the total number of atoms in the supercells. While the central IB-octahedral $O-(Zn,Sb)-O$ layer contains 18 atoms ($2 \times$ Sb, $4 \times$ Zn and $12 \times O$), each added $Zn-O$ layer contributes, regardless of its stacking, an additional 24 atoms (both sides). Depending on n, the supercells thus contain: 42, 66, 90 atoms, .. (for $n = 1,2,3\ldots$).

Prior to the construction of the supercells for the DFT calculations, one needs to handle the discontinuity due to the violation of periodicity along the supercell *A*-axis. There are two ways to address this problem. The first approach, which is commonly used in homologous phases, such as In-doped ZnO [32], is to generate a periodic supercell, where in addition to the head-to-head IB, also a tail-to-tail inversion is generated. However, in Sb-doped ZnO, homologous phases with tail-to-tail segments do not form without the addition of another dopant [31] and therefore this approach is not realistic. Instead, we utilized the second approach, proposed by Yankovich et al. [6], who utilized a slab geometry of finite thickness to model the IB. To calculate such a slab geometry in 3D periodic codes the slabs are separated by a layer of vacuum in the direction of the discontinuity, which also allows unrestrained relaxation of the layers normal to the interface. The width of the vacuum gap needs to be sufficiently large to minimize the strong (tail-to-tail) interactions brought by the nonperiodic features and the artificial polarity inversion. The bulk parts of the slab model were terminated by oxygen. To ensure the formal oxidation states of ions in the supercell (O^{2-}, Zn^{2+}, Sb^{5+}) the stoichiometry is compensated by the addition of an appropriate number of H-atoms on the terminating surfaces, where they saturate the dangling O-ions and form the –OH groups (due to the stoichiometry criterion 50% of the O ions are saturated). Since the dipole, otherwise inherent to noncentrosymmetric crystals, is eliminated by the polarity inversion, no dipole correction is required. The geometry for the IB$_2$ ($n = 8$) model is shown in Fig. 4.

DFT-relaxed wurtzite ZnO was used to construct the supercells for the DFT calculations. Structural relaxation of all the atomic positions was performed. The supercells were optimized for the number of n-layers, sufficient to reduce the influences of the surfaces on the relaxation of the IB, as well as for the width of the vacuum gap necessary to minimize the tail-to-tail interactions. Ideally, the cell parameters at the mid of the ZnO domains ($n/2$) should converge to those of the DFT optimized bulk ZnO. For the convergence test, a sequence of models with an increasing number of ZnO layers ($n = 3,5,7,\ldots$) on both sides of the octahedral IB-layer were generated. After relaxation, the O-O layer widths at the mid section of the ZnO domains, $d'_{O\text{-}O}\,|_{n/2}$, were compared to the corresponding DFT-optimized bulk ZnO, $d^{o}_{O\text{-}O}$ (2.644 Å), reference. The target value of the minimization was to achieve <1 pm difference in $d'_{O\text{-}O}\,|_{n/2}$ - $d^{o}_{O\text{-}O}$; the trend of convergence is shown in the Supplementary material, Fig. S2. These conditions were satisfied for $n = 8$ supercells containing 216 atoms. The starting supercells for DFT calculations have the dimensions: $B = 5.674$ Å, and $C = 9.827$ Å, whereas in the *A*-direction the slab is ~45 Å thick, followed by a 8-Å-wide vacuum gap.

3.4. Transmission electron microscopy

IBs were studied in Sb-doped ZnO ceramics prepared by standard solid-state processing and conventional TEM sample preparation. The ceramics was prepared by mixing reagent-grade powder of ZnO (Pharma A, Union Minier, The Netherlands) with 0.1 mol% of Sb_2O_3 (Merck, Darmstadt, Germany) as the IB-forming additive. Pressed pellets were sintered at 1200 °C for 16 h to produce compact ceramic samples. For the TEM studies the samples were cut into 3-mm discs by an ultrasonic cutter (Sonicut 380, SBT, USA), mechanically thinned to 100 μm and dimpled down to 20 μm in the center (Dimple grinder 656, Gatan Inc., USA). Finally, the TEM samples were obtained by ion-milling with 4-kV Ar+ ions

Table 1
Results of DFT calculations for IB_i models and originating ZnO wurtzite (*w*), stacking fault (SF_i) and sphalerite (*s*) structures, with corresponding Zn-sequences, stacking segments, normalized IB_i energies ($\Delta E_{DFT\text{-}i}$) and energy forecasts ($\Delta E_{f\text{-}cast}$). Relative energies of SF structures are listed relative to wurtzite ZnO [44]. In a similar way, the energy of the most stable IB model (E_{IB3}) is used as a reference for IB structures; where $\Delta E_{DFT\text{-}i} = (E_{IBi} - E_{IB3})/3$ (3 ZnO units per *B-C* plane). Hypothetical IB_6–IB_8 models are constructed for a verification of the partial energy contributions and calculation of $\Delta E_{f\text{-}cast}$ (*see* Tables S1 and S2 in the Supplementary material).

IB model	IB_1	IB_2	IB_3[a]	IB_4	IB_5	IB_6	IB_7	IB_8
Expression	3–3	4–5	5–5	6–5	7–5	7–5	7–5	7–5
cationic sequence	*wsosw*	*wwosw*	*wwoww*	*wwoss*	*wwows*	*swosw*	*swows*	*ssoss*
St. segments	2 × *wso*	*wwo*+*wso*	2 × *wwo*	*wwo*+*sso*	*wwo*+*swo*	*swo*+*wso*	2 × *swo*	2 × *sso*
$\Delta E_{DFT\text{-}i}$ [meV/*f.u.*]	55	24	0	59	36	58	69	118
$\Delta E_{f\text{-}cast}$ [meV/*f.u.*]	52 ± 4	26 ± 3	0 ± 4	59 ± 3	35 ± 3	61 ± 3	69 ± 4	118 ± 3
orignat. stacking	ZnO(*w*)	SF_1[b]	SF_2[b]	SF_3[b]	SF_4[b]			ZnO(*s*)[c]
Expression	1	4–2	5–2	6–2	7–2			2
cationic sequence	-*w*-	*wwsww*	*wwssw*	*wswsw*	*wsssw*			-*s*-
ΔE_{DFT} [meV/*f.u.*][b]	0	15	31	31	47			14

[a] IB_3 ($n = 8$) model with the lowest total energy, used as a reference for other IB structures, this study.
[b] Relative energy contributions of SFs per formula unit; *cf.* ZnO unit-cell area, reported by Yan et al. [46].
[c] Relative energy of sphalerite ZnO (*s*) with respect to the energy of wurtzite ZnO (*w*), this study.

at an incidence angle of 6° to obtain transmissive areas for the TEM investigations. The TEM studies were performed using a 400-kV top-entry high-resolution TEM (4000EX, Jeol Ltd., Japan) and 200-kV field-emission gun (FEG) TEM (2010F, Jeol Ltd., Japan) with an ultra-high-resolution pole piece, both suited for resolving interatomic spacings in two essential projections of ZnO, $[2\bar{1}\bar{1}0]$ and $[01\bar{1}0]$, that are both needed to identify the translation and dopant distribution of the IBs, respectively. The chemical composition of the IBs was examined by energy-dispersive X-ray analysis (EDS), using Si (Li) detector (Link ISIS-300, Oxford Instruments, Abingdon, UK) and a narrow probe (<2 nm) to enhance the signal stemming from the IB [28].

3.5. Quantitative HRTEM analysis

Analysis of the experimental HRTEM images included identification of IB stacking, followed by image simulations for the corresponding IB model using the electron-optical parameters of the microscope. For the 400-kV microscope, $C_s = 0.96$ mm (spherical aberration), $\Delta f = 11$ nm (spread of focus) and $\Theta_c = 0.6$ mrad (beam convergence), while for the 200-kV microscope $C_s = 0.48$ mm, $\Delta f = 8$ nm and $\Theta_c = 1.2$ mrad, respectively. The defocus value was estimated form the contrast transfer function (CTF) of amorphous material from the sample, and crystal thickness calculated from the ion-milling angle and the distance of the region of interest from the crystal edge. For simulations we used a multi-slice algorithm (EMS software [60]) with a plane wave of 1024 × 128 dynamically scattered beams, which gave a sampling resolution of ~5 pm along the *A*- and *B*-directions of the supercells, sufficient to determine the lattice relaxation across the IB plane. Before matching, the experimental images were processed using a Wiener filter script in the DigitalMicrograph® software (Gatan Inc., Warrendale PA, USA) and adjusted for any geometric distortion due to camera plane misalignment. The cross-correlation coefficient (XCC) was used as a measure for matching between the experimental and simulated images. To find the experimental IB relaxation, the starting models were relaxed by a reduction of O–(Zn,Sb)–O width (δ) until the images produced maximum correlation.

4. Results

To date, only the IB_2 model was reported for Sb-doped ZnO [6,8]. In the following assessment we evaluate with DFT calculations whether this model is also the most stable one. The stability of the IB structures differing due to translation (Eqs. 3–7), with the IB-plane chemistry corresponding to Sb-rich IBs [8], was studied using first-principles calculations, and the results of the calculations were verified by quantitative HRTEM analysis of the IBs in Sb_2O_3-doped ZnO ceramics.

4.1. DFT calculations

Following the described computation methodology, convergence is achieved for all models. Relative differences in stabilities of the optimized IB models, by means of minimum energies, are significant and to a certain extent surprising (Table 1). Contrary to all expectations the DFT calculations suggest that IB_2 is not the most stable model. Structurally, it is the O-sublattice that defines the framework of all translations, so it may be that it also defines the stability of the IB structures. As the wurtzite is most stable of the originating structures, one might rightfully expect that IB_1 would then be the most stable among the IB structures, and the rest of the IB models would follow $SF_1 < SF_2 \cong SF_3 < SF_4$ as reported by Yan et al. [46]. However, this is also not the case. Our calculations show that this is not the IB_2 nor the IB_1 model that is the most stable, but the IB_3, followed by $IB_2 < IB_5 < IB_1 < IB_4$, respectively. How can this be explained? It appears that the stability of the IB models does not follow the originating O-stacking. The reason lies in the fact that the Zn-sublattice is translated with inversion, which causes the departure of the cationic stacking from the originating O-stacking sequences, and the stability in fact depends on the cationic and not the anionic stacking. If we scrutinize the cationic stacking over different IB models (Fig. 3), we see that only in the IB_3 model all the cations, except those in the IB plane, are in *hcp* stacking, whereas in all other IB models one or more Zn-layers are in *ccp* stacking. Hence, if any deviation from *hcp* stacking in the Zn-sublattice increases the total energy, it should be possible to observe a correlation between the number of *ccp* sequences and the relative stability. To confirm this assumption, we additionally performed DFT calculation on sphalerite ZnO. Our results show that the total energy of sphalerite ZnO is indeed larger than that of wurtzite ZnO in excess of +14 meV per one formula unit (*f.u.*) of ZnO. This is similar to previously reported values using different computational methodology [46]. The relative energies in Table 1 are listed with respect to reference structures with the lowest energy, *i.e.* pure wurtzite for the SFs, and the IB_3 model for the IBs.

Given that the energy contributions from the bulk ZnO, surfaces and vacuum gaps, as well as those from the octahedral IB-layers, are identical for all IB models, the differences must arise from variations in the Zn-sublattice translation. In a simplified notation (Fig. 3), cationic sequences can be written in terms of the wurtzite tetrahedral (*w*), sphalerite tetrahedral (*s*) and IB octahedral (*o*) sites. The main contributing variations are found on both sides of IB-plane; where the Zn-sublattice either follows regular *hcp* stacking or contains *ccp* disruptions. Each IB model is thus characterized by two contributing stacking segments: one on the left-, and the other on the right-hand side of the IB-plane. For example, the IB_2 model comprises a *wwo* sequence from the left-hand and an *osw* sequence from the right-hand side, therefore, involving one *ccp* layer. Consequently, the total energy of IB_2 is expected to be higher than that of IB_3 with *wwo* segments on both sides of the IB-plane (left and right-hand stacking segments are commutative).

The analysis of the IB models shows that there are four essential stacking segments, *i.e.: wwo, wso, swo* and *sso*, each carrying a specific energy contribution. The contributing stacking segments for all models are listed in Table 1. Each IB model thus represents one independent equation for one or two variables, depending on its stacking. For example, the relative energy of the IB_2 model comprises contributions of the *wwo* and *wso* segments, *i.e.*, $E_{IB2} = E_{wwo}+E_{wso}$, *etc*. In the same way equations can be generated for all the IB models and solved for the unknowns. While 4 models are algebraically sufficient, more models are helpful to determine the energy contributions to a greater precision. When sets of independent linear equations for all the unique combinations are solved, the partial energies of the stacking segments increase in the following order: E_{wwo} (0 ± 2 meV) < E_{wso} (25±2 meV) < E_{swo} (34±2 meV) < E_{sso} (59±2 meV). In our calculations, the *wwo* segment is used as a valid variable, even though its value is expected to be zero owing to the fact that $E_{IB3} = 0$. The *wwo* segment indeed shows the lowest energy converging to zero in all combinations. What is interesting is the difference between the *wso* and *swo* segments. They both contain one *ccp* sequence; however, the cubic bond in the *wso* segment is connected to the cubic octahedral bond, whereas in the *swo* segment the cubic bond transgresses a hexagonal one before the octahedral. Apparently, interlinking the same type of bonds is energetically more favorable than their alternation. As expected, the *sso* segment with two cubic bonds displays the highest energy, nearly that of *wso* and *swo* combined. This shows that depending on their translation state, the energy of the IBs increases with the number of *ccp* sequences as well as with their connectivity. Details of the partial energy calculations are given in the Supplementary materials (Table S1).

The energetic contributions of the stacking segments can now be used to understand and even to forecast the stability ($\Delta E_{\text{f-cast}}$) of the different IB models. To verify the validity of this approach three additional hypothetical models IB_6–IB_8 were constructed. The forecasts based on the energy contributions of the constituting segments have the capacity to predict the relative energies of the IB models. For example, the relative energies of the hypothetical IB_7 (*swows*) and IB_8 (*ssows*) models were first predicted based on partial energies of the stacking segments obtained from the IB_1–IB_6 models. The forecast implied that the *swows* model should show an excess energy of 69 meV/*f.u.* and the *ssoss* model of 117 meV/*f.u.*, respectively. After the DFT optimization the two models showed the excess energies of 69 meV/*f.u.* and 118 meV/*f.u.*, respectively, which validates the use of stacking segments to explain the stability of the IBs. Details on the IB energy forecasts are given in Supplementary materials (Table S2).

If the stacking is expressed in terms of polar vectors, we can show that the energies are proportional to the lengths of the resulting vectors that are a sum of the individual polar O→Zn vectors, $\vec{r}_i$, in each layer of the segments. As their directions alternate depending on the stacking and their lengths differ depending on their position with respect to the IB-plane, their resultants are consequently different. The energy contributions of the stacking segments compared to the corresponding resultant vectors are shown in Fig. 5. We can see that their trends match, within standard deviations, suggesting that the energy contributions do not only depend on the bond lengths but also on their spatial dispersion. The constituting vectors are illustrated in Fig. S3 and listed Table S3 of the Supplementary materials.

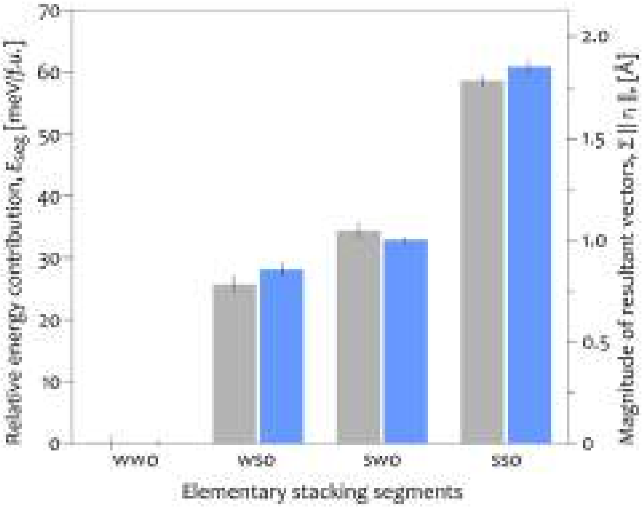

Fig. 5. Comparison between the relative energy contributions (*grey*) and the magnitudes of the resultant vectors (*blue*) for the individual stacking segments. The *wwo* is used as a reference according to $E_{IB3} = 2E_{wwo} = 0$. (For interpretation of the references to color in this figure legend, the reader is referred to the web version of this article.)

Let us now look at the first three IB models; IB_1, IB_2 and IB_3, that are experimentally confirmed in ZnO. With the inversion operation the IB_3 model has the highest possible number of Zn atoms in the *hcp* stacking and thus its energy is the lowest. Slightly worse is the situation in the IB_2 model, where on one side the stacking is hexagonal, while on the other the stacking is cubic. This is reflected in the increase in the total energy that corresponds to the *wso* segment. Finally, the worst situation is observed in IB_1 model, with cubic cationic stacking on both sides of the IB, and the energy corresponding to two *wso* segments. Consequently, the total energies of the IBs ($E_{IB3}<E_{IB2}<E_{IB1}$) are in a reverse order compared to their originating stacking ($E_{SF2}>E_{SF1}>E_{ZnO}$). DFT optimized models can be used to extract deeper structural details. Optimization starts from the supercells with equidistant *cp* O-layers. In this idealized geometry, the Zn–O bond lengths of the tetrahedral Zn-atoms are ~1.98 Å, whereas the (Sb, Zn)–O bond lengths of the octahedrally coordinated cations (IB plane) are ~2.28 Å (Fig. 6a). During relaxation, the initial structures experience high compressive forces pulling the ZnO blocks towards the IB-plane. As a result, the bond lengths are reduced, and the octahedra are flattened. Within variations, the Zn–O bond lengths in IB-plane are 2.21±0.02 Å, while Sb–O are 2.05±0.01 Å, on average (Fig. 6b). In addition to the apparent compression, the octahedral bond lengths are differentiated with respect to the electronic structures of the Zn and Sb, producing periodic undulation (Fig. 6c–d). The reduction of the bond lengths varies slightly for different IB models, but the trend of the compression is general. While the O-sublattice is locally compressed, the Zn-sublattice displays expansion due to the inversion.

Given that IB_2 is the only model known in the literature for Sb-rich IBs in ZnO, our result appears no less than surprising, raising many rightful questions, such as; are DFT calculations to be trusted, if so, are there any other translations possible for Sb-rich IBs in ZnO, what are actual IB translations in other studies, and were there incorrect interpretations of IB stacking in the past. To answer these questions, the IBs in Sb_2O_3-doped ZnO must be

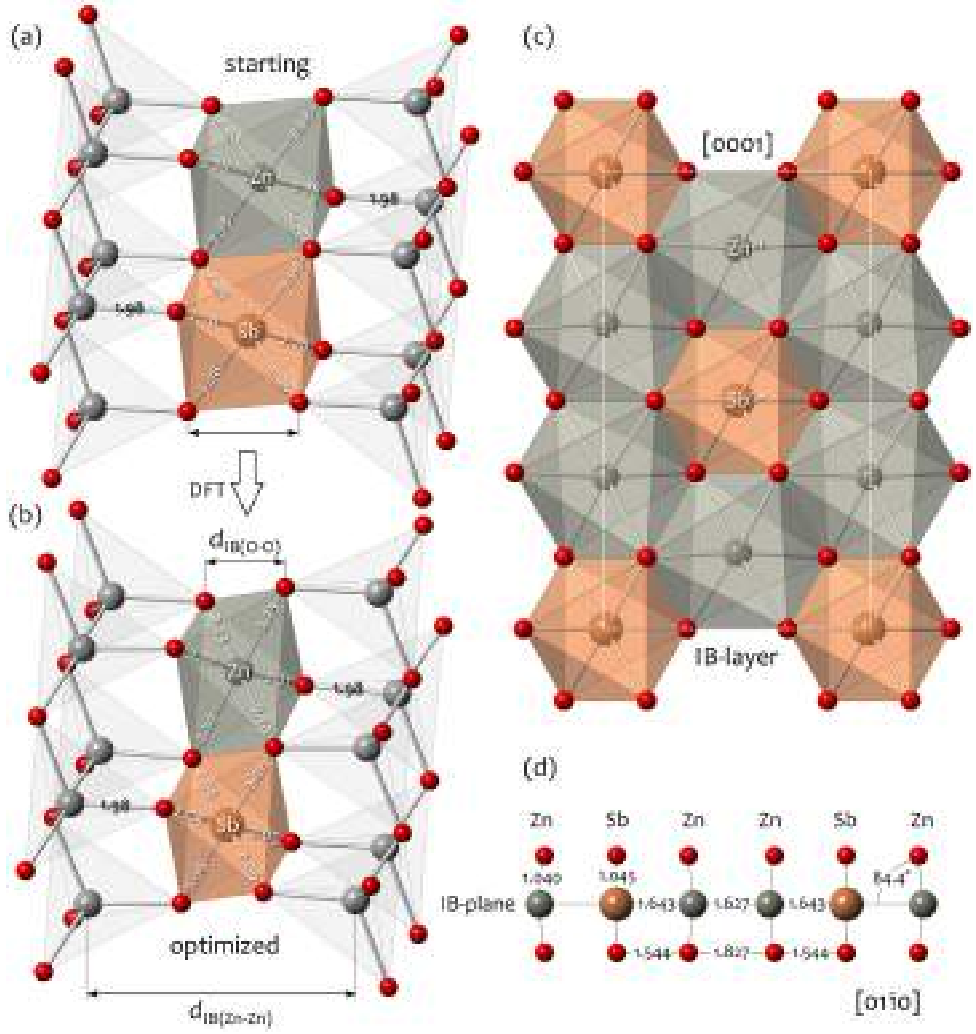

Fig. 6. Bond lengths in the IB layer (**a**) before and (**b**) after DFT relaxation resulting in a lateral contraction of the bulk parts. IB characteristic distances $d_{IB(O\text{-}O)}$ and $d_{IB(Zn\text{-}Zn)}$ defining IB-octahedra width and the distance between the Zn-planes in adjacent domains, respectively. (**c**) IB-layer in [0001]-projection showing a honeycomb distribution of cations (Zn^{2+} and Sb^{5+}). The Sb–O bond lengths are 10% shorter than the corresponding Zn–O bond lengths. (**d**) Undulation of projected bond lengths and torsion angles in IB-plane viewed in $[01\bar{1}0]$.

reexamined experimentally, and the literature carefully scrutinized for possible flaws or misinterpretations.

4.2. HRTEM analysis of IBs

We investigated translation states of basal plane IBs in Sb_2O_3-doped ZnO ceramics using quantitative HRTEM. While cation ordering in the IB-plane is directly visible in the $[01\bar{1}0]$-type projection [8], stacking configuration is best studied in the $[2\bar{1}\bar{1}0]$-type projection. Therefore, ZnO grains near these two zone axes were searched for IBs, and tilted into corresponding projections for HRTEM observation. If crystal orientation is near the halfway between the two zone axes, both projections can be reached within the same ZnO grain. Several IBs were recorded along the thin crystal region for further analysis. HRTEM images of Sb-rich IB are shown in Fig. 7.

To determine the translation across the IBs, we analyzed the lattice images in the $[2\bar{1}\bar{1}0]$ projection. HRTEM images were recorded near the direct contrast transfer condition (Scherzer focus), where the cationic columns appear as black dots in a few-nm-thin crystal. The cationic sequence, and thus the stacking of the parent IB model, can be most directly identified by following these dots across the IB-plane. Analyzing the stacking over several different IBs revealed a surprising fact. Instead of two successive *ccp* sequences, as expected for the IB_2 model [8], we more frequently observe a single *ccp* sequence of cations across the IB (Fig. 7a), corresponding to the IB_3 model. To prove that the IBs are indeed Sb-rich, the presence of Sb in the IB plane was checked by EDS and in-plane ordering in the $[01\bar{1}0]$ projection (Fig. 7b), showing 1:2 cationic ratio, characteristic of Sb-rich IBs [8]. This unexpected observation fully substantiates our DFT analysis, according to which the IB_3 model is the most stable.

4.3. Quantitative HRTEM analysis of IB models

Two experimentally confirmed IB models, IB_2 [8] and IB_3 (this work), are taken into further consideration. Due to the polarity of the structure, the contrast features in the HRTEM images are delocalized and the IB relaxation can thus not be measured directly [8]. Instead, this can be accomplished by cross-correlation of the experimental HRTEM images with the model-based simulations. First, the geometry of the bulk ZnO is adjusted to the DFT cell parameters so that the simulated and experimental images can be compared. To determine the experimental $d'_{IB(O\text{-}O)}$ widths for both IBs we used the $d'_{IB(O\text{-}O)}$ values of the DFT relaxed models as a reference. Then, 10 further IB models were generated by

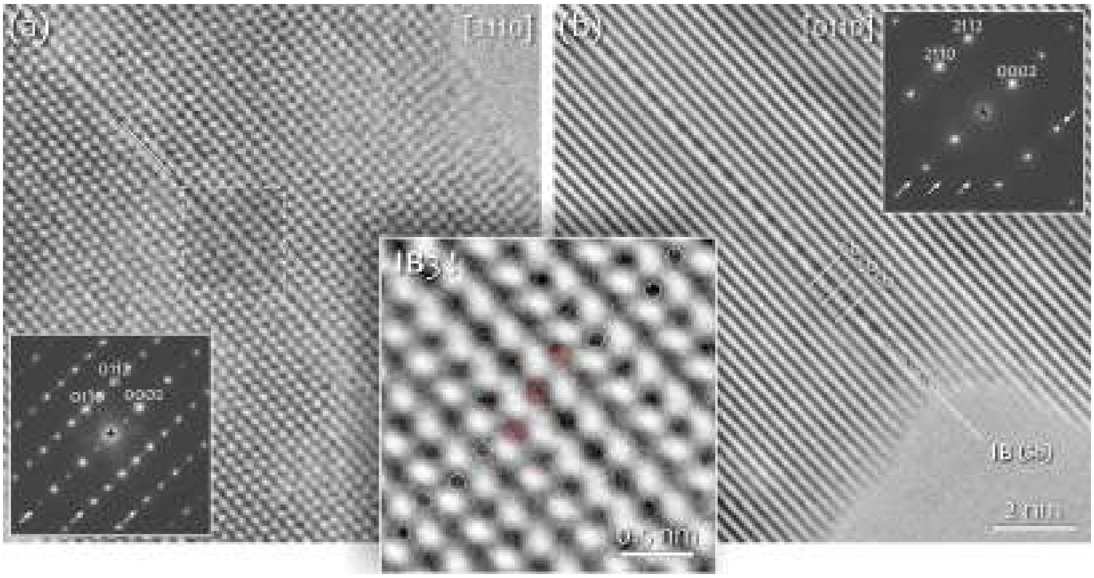

Fig. 7. HRTEM study of IBs in Sb_2O_3-doped ZnO in two low-index crystallographic projections: (**a**) $[2\bar{1}\bar{1}0]$ and (**b**) $[01\bar{1}0]$, with the corresponding electron diffraction patterns. IBs are characterized by lateral expansion due to the inversion of polarity. Black dots in HRTEM images correspond to cation columns, allowing to track the stacking sequence in (a), and cation ordering in (b). Close-up of HRTEM image in the $[2\bar{1}\bar{1}0]$ projection clearly shows a stacking configuration with a single ccp sequence (*red* circles) across the IB plane (IB_3). (For interpretation of the references to color in this figure legend, the reader is referred to the web version of this article.)

subtracting/adding 2.5-pm gaps on both sides of the IB-plane, each producing different widths of the IB octahedra in order to match the experimental value. Generated models covered the $d'_{IB(O\text{-}O)}$ widths from –25 to +25 pm, with a 5-pm steps discrepancy (δ), from the DFT reference. Based on these models simulated images were computed and compared to experimental HRTEM images. The resulting XCC values plotted as a function of δ show parabolic dependence; XCC=$f(\delta)$, (Fig. 8). The vertical XCC offset (0.941 *vs.* 0.947) does not play a significant role in the determination of the experimental δ values and depends principally on the quality of the HRTEM images. The maxima of the XCC curves, $\delta|_{df(\delta)/d\delta=0}$, represent the IB models with matching $d'_{IB(O\text{-}O)}$ contraction, which in both cases nearly coincides with the $d'_{IB(O\text{-}O)}$ reference values for IB_2 and IB_3 obtained with the DFT calculations. The discrepancies of +0.82 pm and +0.45 pm for IB_2 and IB_3, respectively, calculated using a derivation of the parabolic functions, in fact show some systematic underestimation of $d_{IB(O\text{-}O)}$ by DFT, but these values are way below the accuracy threshold of >5 pm, achievable by quantitative HRTEM analysis [61].

Fig. 9 shows HRTEM images of the IB_2 and IB_3 structures, both observed in Sb-doped ZnO, with overlaid simulated images based on DFT-optimized models. Under given electron-optical conditions the cations coincide with the black dots in the HRTEM images, which makes IB translation modes easy to identify. A good match between the experimental HRTEM images and the simulations based on the DFT-relaxed models for both IB models is quite astonishing, and additionally confirms the validity of the predicted IB models. All the essential structural details, such as stacking and the apparent IB expansion, are well reproduced. This gives us the confidence to analyze further structural elements directly from the DFT-optimized models below the 5 pm (~1 bohr) limit.

Before quantifying the structural features, we first consider the accuracy of the DFT-optimized models. This is defined by the difference between the O-O width at the mid of ZnO domains ($d'_{O\text{-}O}|_{n/2}$) in the relaxed supercell model and that in the relaxed bulk ZnO ($d^{o}_{O\text{-}O}$). For $n = 8$ supercells, $d'_{O\text{-}O}|_{n/2} = 2.651$ Å. Fig. 10 illustrates the variation of the layer widths with their distance from the IB-layer ($n = 0$). Larger variations can be observed in the O-sublattice, which shows a net expansion of ~2.0 pm after the IB-layer ($n = 1$), that drops to ~0.6 pm at the fourth layer ($n = 4$) and remains constant outwards (±0.1 pm). Variations in the Zn-sublattice are larger (±0.6 pm), while only a small net expansion is

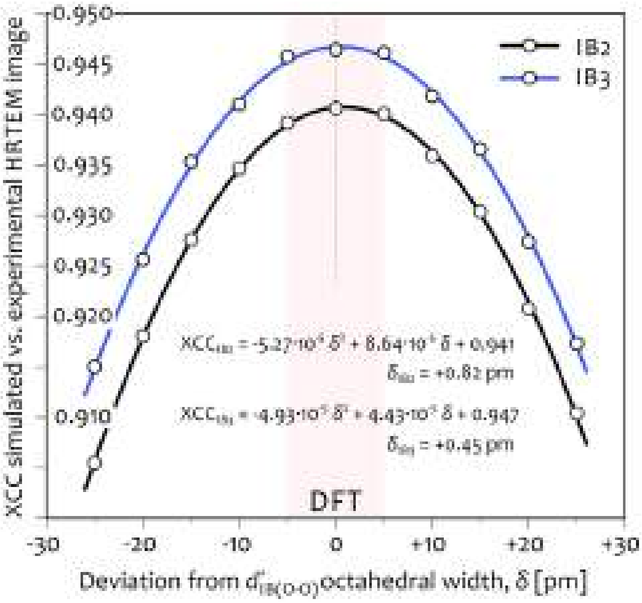

Fig. 8. Parabolic dependence of cross-correlation coefficient (XCC) between experimental HRTEM images and model-based HRTEM simulations *vs.* IB relaxation $d'_{IB(O\text{-}O)}+\delta$ for IB_2 (*black* curve) and IB_3 (*blue* curve). $d'_{IB(O\text{-}O)}$ widths of DFT relaxed models are used as a reference (0 pm deviation) from which the models with different IB relaxation were generated to match the experimental $d'_{IB(O\text{-}O)}$ (maxima of the XCC curves). Both maxima are shifted slightly to positive δ values. XCC dependencies are shown as parabolic functions of the deviation δ. (For interpretation of the references to color in this figure legend, the reader is referred to the web version of this article.)

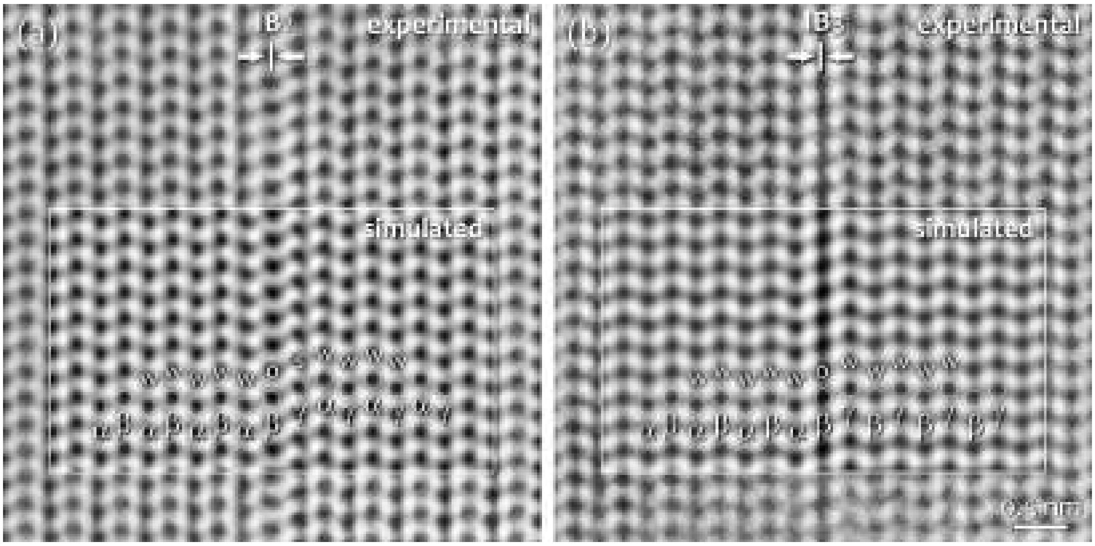

Fig. 9. Experimental HRTEM images of IBs in the $[2\bar{1}\bar{1}0]$ projection with stacking sequences corresponding to the (**a**) IB_2 and (**b**) IB_3 configurations; the insets (outlined) are simulated HRTEM images based on the DFT relaxed IB_2 and IB_3 models, respectively. Cationic stacking (*red*) is indicated above the sequence for reference.

observed towards the IB-plane and outwards. The variations in the layer widths (d) are a consequence of the expansive forces caused by the highly charged cations in the IB plane and the presence of the vacuum gap needed to accommodate the reverse tail-to-tail polarity. These two boundary effects cause a net expansion of the bulk ZnO parts.

Compared to $d^{o}_{O\text{-}O}$ = 2.644 Å of the DFT-relaxed ZnO, the net difference is +0.6 pm for both IB models, which is below our <1 pm target. This value represents the accuracy limit of the optimized DFT models. Another effect that can be observed when comparing both models is the asymmetry in the layer widths due to additional *ccp* stacking in IB_2 compared to IB_3 with a superior symmetry.

IB relaxation is commonly characterized by the so-called 'IB expansion' [6,8], which is observed in the cation sublattice due to the head-to-head polarity inversion, where Zn atoms swap from the Type-I to Type-II tetrahedral sites. In a geometric case, the net expansion of the Zn-sublattice, $\Delta_{IB(Zn\text{-}Zn)}$, corresponds to twice the u-parameter and hence $d_{IB(Zn\text{-}Zn)}$ = (½+2u) d_c = 6.582 Å, while $d_{IB(O\text{-}O)}$ = ½ d_c = 2.604 Å, expressed in terms of the ZnO unit-cell parameters [43]. In actual IBs, however, where the octahedral IB-layers are flattened (*i.e.* $d_{IB(O\text{-}O)} < ½d_c$), the cation sublattice 'IB expansions' are accordingly smaller. Given the accuracy of the DFT optimization, the characteristic IB widths can be evaluated directly from the relaxed models. IB widths resulting from quantitative HRTEM analysis and DFT optimization, normalized to the unit-cell parameters of ZnO are listed in Table 2 and compared to the reported values.

Within the accuracy ranges of the quantitative HRTEM (±5 pm) and DFT (±1 pm) methods the apparent Zn-sublattice expansion $\Delta_{IB(Zn\text{-}Zn)}$ for the IB_2 and IB_3 models expressed in real-space distances are +81 pm and +77 pm, whereas the corresponding O-sublattice contractions $\Delta_{IB(O\text{-}O)}$ are –53 pm and –57 pm, respectively. The larger value of the IB expansion for the IB_2 model can be attributed to the presence of *ccp* staking (*wso*) and is consistent with the larger bond lengths in the sphalerite modification of ZnO.

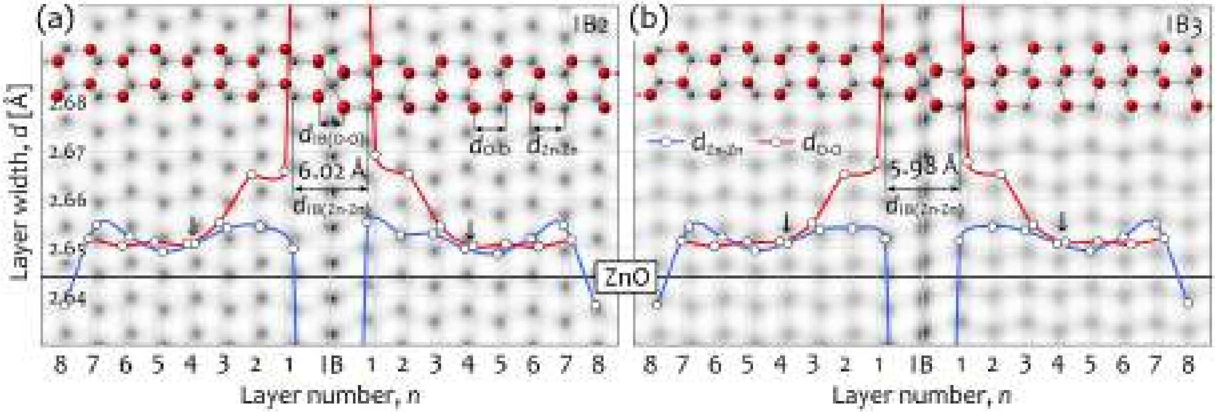

Fig. 10. Variations in the $d_{Zn\text{-}Zn}$ and $d_{O\text{-}O}$ widths as a function of distance (expressed in n) from the IB-plane in DFT-optimized: (**a**) IB_2 and (**b**) IB_3 models. Overlaid models and HRTEM images (in background) facilitate the identification of the layer sequence. Solid black line is the reference $d^{o}_{O\text{-}O}$ (2.644 Å) in DFT-relaxed ZnO.

Table 2

Measured and calculated IB widths, $d_{IB(Zn\text{-}Zn)}$, for IB$_2$ and IB$_3$ models compared to experimental and theoretical literature data. Sublattice $\Delta_{IB(Zn\text{-}Zn)}$ expansion and $\Delta_{IB(O\text{-}O)}$ contraction are expressed in fractions of the *c*-parameter of ZnO ($c = 5.207$ Å) [43] through the following relations: $\Delta_{IB(Zn-Zn)} = [d_{IB(Zn\text{-}Zn)} - c]/c$ and $\Delta_{IB(O\text{-}O)} = \Delta_{IB(Zn-Zn)} + 0.5 - 2u$.

IB model: method	$d_{IB(Zn-Zn)}$ [Å]	$\Delta_{IB(Zn-Zn)}$	$\Delta_{IB(O\text{-}O)}$	u^*	Reference
IB$_2$: HRTEM	6.46	+0.24	–0.024	0.382	McCoy et al. (1996) [26]
q-HRTEM	6.05 ± 0.05	+0.162	–0.102	0.382	Rečnik et al. (2001) [8]
HAADF-STEM	5.99 ± 0.04	+0.150	–0.113	0.382	Yankovich et al. (2012) [6]
q-HRTEM	6.03 ± 0.05	+0.158	–0.105	0.382	this work (Fig. 8)
DFT slab	6.12	+0.175	–	–	Yankovich et al. (2012)[6]
DFT periodic	6.03	+0.158	–	–	Yankovich et al. (2012) [6]
DFT vac. gap	6.02 ± 0.01	+0.156	–0.102	0.379	this work (Fig. 10a)
IB$_3$: DFT vac. gap	5.98 ± 0.01	+0.148	–0.110	0.379	this work (Fig. 10b)
q-HRTEM	5.99 ± 0.05	+0.149	–0.115	0.382	this work (Fig. 8)

* u values in DFT-relaxed models are not available in [6], thus only the $\Delta_{IB(Zn-Zn)}$ expansion is listed.

5. Discussion

IBs are growth defects [7] that form as a result of 2D topotaxial reaction between ZnO and specific metal oxides along the basal [2,8] or pyramidal planes [4,32–40,49]. Formed with so many different dopants, IBs present an ideal model system to study the formation of extended defects in layered structures. In our study, we address Sb-rich IBs that are related to manifold physical phenomena such as, conduction nonlinearity [1,9–11], grain-growth control [7,12–14], electron and phonon transport [3], and recently, the origin of as yet unexplained p-type conduction in ZnO [5,6,15–19]. As planar defects importantly define the physical properties of semiconductors knowing their exact structure has become imperative for resolving the origin of these phenomena [62,63].

The first lattice images of IBs in Sb_2O_3-doped ZnO were reported by Kim and Goo [21], who anticipated a dopant-free interface. Due to the ambiguity of the atomic positions in their images the type of translation is inconclusive, nevertheless they reported a –57 pm lattice contraction in the boundary region, which is consistent with O-sublattice contraction of IB$_3$ of our study. McCoy et al. [26] determined the IB$_2$ configuration, with cation displacement of $+0.24c$, which is close to the geometric IB width ($1–2\ u$) with no relaxation. Employing quantitative HRTEM analysis in two projections, Rečnik et al. [8] finally solved the local structure and the chemistry of Sb-rich IB. The translation of their IB, and the values of Zn- and O-sublattice relaxations are consistent with those for IB$_2$ model in our study. In addition to $\Delta_{IB(Zn-Zn)}$ and $\Delta_{IB(O\text{-}O)}$ relaxations, other fine structural details, such as O-undulation caused by the honeycomb arrangement of Sb and Zn atoms along the IB-plane visible in their experimental images (Fig. 6b [8]) are reproduced in DFT-relaxed IB structure (Fig. 6d, present work). Given the accuracy of HRTEM analysis, the Rečnik's model was ever since considered as the reference model for Sb-rich IBs in ZnO [6,29,31]. The importance of accurate structural determination of extended defects in semiconducting materials has been recently pointed out by Lançon et al. [63] in *ab-initio* study of inversion domain boundaries (IDBs) in GaN, where they achieved the ±0.1 pm match between the experimental and the computational displacements.

The structure of Sb-rich IBs thus appeared to have been solved back in 2001 [8], and no subsequent study had challenged the conclusions of this work. In order to verify whether this model is indeed the most stable one, we reconstructed the Rečnik's model, and four other models based on possible departures from the regular wurtzite stacking [46] for comparison. In all the models, the inversion is achieved by the translation of Zn^{2+} from Type-I to Type-II tetrahedral sites in the adjacent domain [7,8]. The resulting IB models were optimized using DFT calculations. Contrary to all expectations, we found that the generally accepted IB$_2$ model based on the SF$_1$ sublattice [8] is not the most stable of the considered models. Our calculations have shown that IB$_2$ has the second lowest energy, whereas the most stable of all the models is the IB$_3$ model, based on the SF$_2$ sublattice, with 24.3 meV/*f.u.* lower total energy compared to the IB$_2$. Our systematic HRTEM study of Sb_2O_3-doped ZnO confirmed that IB$_3$ are indeed more common, and only here and there we find one with the IB$_2$ translation, which means that Rečnik et al. [8] in fact studied the less frequent type of the two. This outcome is quite surprising since the formation energy of SF$_2$ is almost twice as high as that of SF$_1$ [46], and their incidence is consequently low. Given the new insights, the question arises why IB$_3$ are possible at all, and how the two types of IBs can coexist?

During examination of the samples for IBs, we captured several SFs, including their transitions from wurtzite to SF and from one type of SF to another. This gave us the opportunity to reconstruct the formation of SFs and IBs. According to the theoretical calculations by Yan et al. [46], SF$_1$, containing one *ccp* layer, is thermodynamically the most favorable type of SF in wurtzite ZnO. Any SF, that involves additional *ccp* sequences would have proportionally higher formation energy and is less likely to form. In line with the reported formation energies [46], our HRTEM observations confirm, that SF$_1$s are very common in ZnO, whereas SF$_2$s are rare. Based on their modalities within the ZnO crystal, we can resolve their mutual relation and the underlying formation mechanism. While SF$_1$s form directly from wurtzite, SF$_2$s do not, and need a preexisting SF$_1$, which explains their lower incidence. The reason why SF$_2$ always forms from SF$_1$ rather than from the pure wurtzite lies in the fact that it is energetically less demanding to generate SF$_2$ through two successive ⅓$[01\bar{1}0]$ glides, rather than make one full ⅔$[01\bar{1}0]$ glide at once, which would be necessary if SF$_2$ would form directly from the wurtzite. Crystallographically, removal or insertion of a *cp* plane in a *hcp* sequence gives the same result and the origin of SFs cannot be rationalized. However, their genesis can be deduced from their relation with the host. From lattice images of ZnO we thus observe that SF$_1$s are always extrinsic (*cp*-plane insertion), whereas SF$_2$s are intrinsic (*cp*-plane removal). The samples produced with higher mechanical load prior to sintering would generally display a higher density of SFs [64]. Other types of SFs, predicted by Yan et al. [46], were not observed in our samples.

Now, let us see why IB$_3$, based on the less frequently occurring SF with higher formation energy, is more likely to form. The answer to this question lies in the cationic sequence of the particular IB structure and related energy contributions. In a theoretical study of SFs, Yan et al. [46] found a simple relation between the increase in the total energy and the number of cubic bonds. If this rule is applied to IBs, we find that owing to inversion, the cation stacking of the SF$_2$ structure with two *ccp* sequences is reshuffled in a way that the resulting IB$_3$, ends up with only one *ccp* sequence and correspondingly the lowest total energy of all the IB models. On the other hand, IB_2 gains one *ccp* sequence in the cation sublattice, with respect to its parent SF_1, and therefore compared to IB_3, its total energy is correspondingly higher. The worst is the situation for IB_1, which after the inversion acquires as much as three *ccp* sequences in the cation sublattice, from *none* in the originating wurtzite structure. For the near-equilibrium system containing SFs and IBs, it is therefore more favorable to have a combination of SF_1 (+15 meV/*f.u.*) and IB_3 (0 meV/*f.u.*), rather than the energetically expensive SF_2 (+31 meV/*f.u.*) and IB_2 (+24 meV/*f.u.*).[1] Namely, the $SF_2 \rightarrow IB_3$ transition more efficiently reduces the system energy than the $SF_1 \rightarrow IB_2$ transition, and thus it is more likely that IB_3 would form, as long as SF_2s are present in host ZnO. In the IB nucleation study, Rečnik et al. [7] showed that in Sb_2O_3-doped ZnO ceramics, every ZnO grain contains only one IB, which is usually the one that forms first. Therefore, if at least one SF_2 is present in the ZnO grain, IB_3 would be the preferred type. In our HRTEM investigation the presence of SF_2s was confirmed. Although SF_2s might be rare compared to SF_1s, the former would be favored for the nucleation of IBs.

The IB_3 type of inversion is in fact more common in Sb-doped ZnO than thought previously. If we carefully reexamine the literature we may observe that many studies referring to Rečnik's model in fact had IB_3 inversion. In the DFT study of Sb-rich IBs in ZnO nanowires by Yankovich et al. [6], investigating their relation to the p-type conduction of ZnO analyzed the IB_2 model. In support of their DFT study they provide high-resolution HAADF-STEM images of IBs close to the nanowire surface, which clearly corresponds to the IB_3 translation, and also explains slightly lower experimental Zn-sublattice expansion compared to their DFT results. The work of Yankovich et al. [6] thus provides the first experimental evidence of the existence of IB_3 translation in Sb_2O_3-doped ZnO. The higher probability of IB_3 stacking in Sb_2O_3-doped ZnO is further supported by the crystallographic study of Garling et al. [31], who showed by Rietveld and HAADF-STEM analyses that the stacking in head-to-head sections of the $Sb_{1/3}Zn_{1/3}GaO_3(ZnO)_3$ phase corresponds to IB_3, as reported for other dopants, including In^{3+}, Fe^{3+} and Sn^{4+} [33–40]. They also showed that head-to-head inversion is accomplished by the incorporation of Sb^{5+} and Zn^{2+} ions in the arrangement reported earlier by the Rečnik [8] and Yankovich groups [6,30], whereas tail-to-tail inversion is stabilized by a full layer of Ga^{3+}.

In the context of recent investigations of Sb-doped ZnO our study is also important from the aspect of the IB stability, which shows that single IBs in ZnO are thermodynamically stable chemically induced planar defects that present a preparatory stage in the formation of layered structures [31], and as such they significantly modulate the physical properties of ZnO [6]. It is not yet clear what exactly is the role of IBs in electron transport and phonon scattering, but nonetheless understanding their exact electronic structure is a step towards resolving these phenomena.

6. Conclusions

Combining atomistic modeling, DFT calculations and HRTEM investigations we provide a new fundamental insight into the structure and stability of IBs in the Sb_2O_3-ZnO system. Five hypothetical IB models were derived from the known stacking sequences in wurtzite structure, one of which, with a stacking sequence of $A\beta{-}B\alpha{-}A\beta C{-}\gamma A{-}\alpha C$ (IB_2), was previously reported for Sb-rich IB in ZnO and was expected to have the lowest total energy. First-principles calculations based on DFT, revealed that a different model, with a stacking sequence of $A\beta{-}B\alpha{-}A\beta C{-}\gamma B{-}\beta C$ (IB_3), is the most stable for Sb-doping. This unexpected outcome necessitated reinvestigation of IBs in Sb-doped ZnO.

Based on the systematic quantum chemical and atomic-scale microscopy studies of IBs in Sb_2O_3 doped ZnO the following issues were resolved:

(1) The stability of the IB structures depends on the cationic stacking sequence and is proportional to the number of cubic bonds in the constituting stacking segments, whereas anionic stacking does not matter. Partial energies of the segments can be used to predict the relative stability of the new hypothetical models. The stabilities of IBs (derived from parent O-sublattice) follow the sequence: $IB_3(SF_2) < IB_2(SF_1) < IB_5(SF_4) < IB_1(WZ) < IB_4(SF_3)$.
(2) As a reference for the cubic bond energy contribution, the total energy of the sphalerite-type ZnO was calculated to be +14 meV/*f.u.* higher than that of the wurtzite-type ZnO.
(3) Investigating the stacking of several dozen IBs we showed not only that the predicted IB_3 actually exists, but that it is also the prevailing configuration of IBs in Sb_2O_3-doped ZnO. Quantitative HRTEM analysis further showed that other structural parameters such as lattice expansions and local atomic relaxations are accurately predicted by DFT.
(4) Within the accuracy range of the quantitative HRTEM (±5 pm) and DFT (±1 pm), the apparent Zn-sublattice expansion $\Delta_{IB(Zn\text{-}Zn)}$ for IB_2 and IB_3 are +81 pm and +77 pm, whereas the corresponding O-sublattice contractions $\Delta_{IB(O\text{-}O)}$ are −53 pm and −57 pm, respectively. The reliability in determination of local relaxations achieved by DFT method is better than 1 pm.
(5) We show that SF_1 (+15 meV/*f.u.*) and IB_3 (0 meV/*f.u.*) are preferred over the energetically more expensive SF_2 (+31 meV/*f.u.*) and IB_2 (+24.3 meV/*f.u.*), which is indicative of the higher probability of forming IB_3 in Sb-doped ZnO rather than IB_2.

In the present work, a new model of IBs for Sb-doped ZnO was predicted by first-principles calculations and experimentally confirmed by HRTEM. While the knowledge of their precise atomistic structure may help to solve series of open questions, including the role of IBs in the electron transport, phonon scattering, p-type conduction of ZnO, preferences of certain dopants to generate specific structural variants and their formation mechanisms, the excellent match between calculations and experiment demonstrates the power of first-principles calculations when it comes to reproducing the structural features <1 pm precision, and further to predicting related physical properties. Linking the two faces of interface phenomenon, as demonstrated in our study, makes theoreticians and experimentalists to work hand in hand in solving fundamental materials science problems.

Declaration of Competing Interest

The authors declare that they have no known competing financial interests or personal relationships that could have appeared to influence the work reported in this paper.

Acknowledgments

This study is based on part of the Ph.D. thesis of Vesna Ribić. The authors gratefully acknowledge the NSC cluster at IJS (Ljubljana) for the access and continuous support. We thank Dr. Paul McGuiness for proofreading the article, Tina Radošević from the Department for Nanostructured Materials for the TEM sample preparation and Center for Electron Microscopy and Microanalysis (CEMM) from the JSI for the access to the electron microscopy facilities. This work was supported by the Ministry of Education,

---

[1] Energies are relative to the reference low energy structures; SFs *vs.* WZ, and IBs *vs.* IB_3.

Science and Technological Development of the Republic of Serbia (Grant No. 451-03-68/2020-14/200053), the Slovenian Research Agency (Program No. P2-0084) and the Serbian–Slovenian bilateral Project BI-RS/18-19-026: 'Stability via doping: Experimental and theoretical design of functional oxide ceramics'.

Supplementary materials

Supplementary material associated with this article can be found, in the online version, at doi:10.1016/j.actamat.2020.08.035.

References

[1] B.A. Haskell, S.J. Souri, M.A. Helfand, Varistor behavior at twin boundaries in ZnO, J. Am. Ceram. Soc. 82 (8) (1999) 2106–2110, doi:10.1111/j.1151-2916.1999.tb02048.x.

[2] J. Hoemke, E. Tochigi, T. Tohei, H. Yoshida, N. Shibata, Y. Ikuhara, Y. Sakka, Inversion domain boundaries in Mn and Al dual-doped ZnO: atomic structure and electronic properties, J. Am. Ceram. Soc. 100 (2017) 4252–4262, doi:10.1111/jace.14931.

[3] K. Park, J.K. Seong, S. Nahm, Improvement of thermoelectric properties with the addition of Sb to ZnO, J. Alloy. Comp. 455 (2008) 331–335, doi:10.1016/j.jallcom.2007.01.080.

[4] E. Guilmeau, P. Díaz-Chao, O.I. Lebedev, A. Rečnik, M.C. Schäfer, F. Delorme, F. Giovannelli, M. Košir, S. Bernik, Inversion boundaries and phonon scattering in Ga : znO thermoelectric compounds, Inorg. Chem. 56 (2017) 480–487, doi:10.1021/acs.inorgchem.6b02354.

[5] K.C. Pradel, J. Uzuhashi, T. Takei, T. Ohkubo, K. Hono, N. Fukata, Investigation of nanoscale voids in Sb doped p-type ZnO nanowires, Nanotechnology 29 (33) (2018) 335204–335208, doi:10.1088/1361-6528/aac8c8.

[6] A.B. Yankovich, B. Puchala, F. Wang, J.-H. Seo, D. Morgan, X. Wang, Z. Ma, A.V. Kvit, P.M. Voyles, Stable p-type conduction from Sb-decorated head-to-head basal plane inversion domain boundaries in ZnO nanowires, Nano Lett. 12 (2012) 1311–1316, doi:10.1021/nl203848t.

[7] A. Rečnik, N. Daneu, S. Bernik, Nucleation and growth of basal-plane inversion boundaries in ZnO, J. Eur. Ceram. Soc. 27 (2007) 1999–2008, doi:10.1016/j.jeurceramsoc.2006.06.006.

[8] A. Rečnik, N. Daneu, T. Walther, W. Mader, Structure and chemistry of basal-plane inversion boundaries in Sb_2O_3-doped ZnO, J. Am. Ceram. Soc. 84 (11) (2001) 2657–2668, doi:10.1111/j.1151-2916.2001.tb01068.x.

[9] M. Matsuoka, Nonohmic properties of zinc oxide ceramics, Jpn. J. Appl. Phys. 10 (6) (1971) 736–746, doi:10.1143/JJAP.10.736.

[10] D.R. Clarke, The microstructural location of the intergranular metal oxide phase in a zinc oxide varistor, J. Appl. Phys. 49 (4) (1978) 2407–2411, doi:10.1063/1.325135.

[11] D.R. Clarke, Varistor ceramics, J. Am. Ceram. Soc. 82 (3) (1999) 485–502, doi:10.1111/j.1151-2916.1999.tb01793.x.

[12] N. Daneu, A. Rečnik, S. Bernik, Grain growth control in Sb_2O_3-doped zinc oxide, J. Am. Ceram. Soc. 86 (8) (2003) 1379–1384, doi:10.1111/j.1151-2916.2003.tb03479.x.

[13] S. Bernik, N. Daneu, A. Rečnik, Inversion boundary induced grain growth in TiO_2 or Sb_2O_3 doped ZnO-based varistor ceramics, J. Eur. Ceram. Soc. 24 (2004) 3703–3708, doi:10.1016/j.jeurceramsoc.2004.03.004.

[14] A. Rečnik, S. Bernik, N. Daneu, Microstructural engineering of ZnO-based varistor ceramics, J. Mater. Sci. 47 (2012) 1655–1668, doi:10.1007/s10853-011-5937-2.

[15] H.Y. Liu, N. Izyumskaya, V. Avrutin, Ü. Özgür, A.B. Yankovich, A.V. Kvit, P.M. Voyles, H. Morkoç, Donor behavior of Sb in ZnO, J. Appl. Phys. 112 (2012) 033706 –6, doi:10.1063/1.4742984.

[16] J.K. Liang, H.L. Su, C.L. Kuo, S.P. Kao, J.W. Cui, Y.C. Wu, J.C.A. Huang, Structural, optical and electrical properties of electrodeposited Sb-doped ZnO nanorod arrays, Electrochim. Acta 125 (2014) 124–132, doi:10.1016/j.electacta.2014.01.029.

[17] Ü. Özgür, Ya.I. Alivov, C. Liu, A. Teke, M.A. Reshchikov, S. Doğan, V. Avrutin, S.-J. Cho, H. Morkoç, comprehensive review of ZnO materials and devices, Appl. Phys. Rev. 98 (2005) 041301, doi:10.1063/1.1992666.

[18] A.M. Alsmadi, B. Salameh, L.L. Kerr, K.F. Eid, Influence of antimony doping on the electronic, optical and luminescent properties of ZnO microrods, Phys. B: Cond. Matter 545 (2018) 519–526, doi:10.1016/j.physb.2018.07.007.

[19] L. Qi, Z. Chai, H. Yang, M.B. Shahzad, Y. Qi, A facile and reproducible synthesis of non-polar ZnO homojunction with enlarged rectification rate and colorful light emission, J. Alloys Compd. 793 (2019) 295–301, doi:10.1016/j.jallcom.2019.04.109.

[20] M. Trontelj, V. Kraševec, The microstructure of Sb-doped ZnO Ceramics, Sci. Ceram. 14 (1988) 915–920.

[21] J.C. Kim, E. Goo, Inversion twin boundaries in zinc oxide, J. Am. Ceram. Soc. 73 (1990) 877–884, doi:10.1111/j.1151-2916.1990.tb05129.x.

[22] J.C. Kim, E. Goo, Morphology and formation mechanism of the pyrochlore phase in ZnO varistor materials, J. Mater. Sci. 24 (1989) 76–82, doi:10.1007/BF00660935.

[23] V. Kraševec, M. Trontelj, L. Golič, Transmission electron microscope study of antimony-doped zinc oxide ceramics, J. Am. Ceram. Soc. 74 (4) (1991) 760–766.

[24] T. Senda, R.C. Bradt, Twinning in ZnO ceramics with Sb_2O_3 additions, Nippon Seramikkusu Kyokai Gakujutsu Ronbunshi 99 (9) (1991) 727–731, doi:10.2109/jcersj.99.727.

[25] J. Bruley, U. Bremer, V. Kraševec, Chemistry of basal plane defects in zinc oxide – antimony oxide (0.1 mol%) ceramics, J. Am. Ceram. Soc. 75 (11) (1992) 3127–3128, doi:10.1111/j.1151-2916.1992.tb04397.x.

[26] M.A. McCoy, R.W. Grimes, W.E. Lee, Inversion domain boundaries in ZnO ceramics, J. Mater. Res. 11 (8) (1996) 2009–2019, doi:10.1557/JMR.1996.0253.

[27] W. Mader, A. Rečnik, Determination of crystal polarity by electron diffraction from thin crystals, Phys. Status Solidi A 166 (1998) 381–395, doi:10.1002/(SICI)1521-396X(199803)166:1⟨381::AID-PSSA381⟩3.0.CO;2-R.

[28] T. Walther, N. Daneu, A. Rečnik, A new method to measure small amounts of solute atoms on planar defects and application to inversion domain boundaries in doped zinc oxide, Interface Sci. 12 (2004) 267–275, doi:10.1023/B:INTS.0000028656.12913.8a.

[29] T. Yamazaki, N. Nakanishi, A. Rečnik, M. Kawasaki, K. Watanabe, M. Čeh, M. Shiojiri, Quantitative high-resolution HAADF–STEM analysis of inversion boundaries in Sb_2O_3-doped zinc oxide, Ultramicroscopy 98 (2004) 305–316, doi:10.1016/j.ultramic.2003.08.023.

[30] R. Jacobs, B. Zheng, B. Puchala, P.M. Voyles, A.B. Yankovich, D. Morgan, Counterintuitive reconstruction of the polar O-terminated ZnO surface with zinc vacancies and hydrogen, J. Phys. Chem. Lett. 7 (22) (2016) 4483–4487, doi:10.1021/acs.jpclett.6b02174.

[31] J. Garling, W. Assenmacher, H. Schmid, P. Longo, W. Mader, Real structure of$(Sb_{1/3}Zn_{2/3})GaO_3(ZnO)_3$, a member of the homologous series $ARO_3(ZnO)_m$ with ordered site occupation, J. Solid State Chem. 258 (2018) 809–817, doi:10.1016/j.jssc.2017.12.008.

[32] M.A. McCoy, R.W. Grimes, W.E. Lee, Planar intergrowth structures in the ZnO–In_2O_3 system, Philos. Mag. A 76 (6) (1997) 1187–1201.

[33] Y. Yan, J.L.F. Da Silva, S.-H. Wei, M. Al-Jassim, Atomic structure of In_2O_3–ZnO systems, Appl. Phys. Lett. 90 (2007) 261904 –3, doi:10.1063/1.2751596.

[34] J.L.F. Da Silva, Y. Yan, S.-H. Wei, Rules of structure formation for the homologous $InMO_3(ZnO)_n$ compounds, Phys. Rev. Lett. 100 (2008) 255501, doi:10.1103/PhysRevLett.100.255501.

[35] A. Walsh, J.L.F. Da Silva, Y. Yan, M.M. Al-Jassim, S.-H. Wei, Origin of electronic and optical trends in ternary $In_2O_3(ZnO)_n$ transparent conducting oxides (n=1,3,5): hybrid density functional theory calculations, Phys. Rev. B 79 (2009) 073105, doi:10.1103/PhysRevB.79.073105.

[36] A. Goldstein, S. Andrews, R. Berger, V. Radmilović, J. Neaton, P. Yang, Zigzag IDBs in indium-ZnO-based nanowires: structure and formation, ACS Nano 7 (12) (2013) 10747–10751, doi:10.1021/nn403836d.

[37] T. Walther, F. Wolf, A. Rečnik, W. Mader, Quantitative microstructural and spectroscopic investigation of IDBs in sintered ZnO/Fe, Int. J. Mat. Res. 97 (7) (2006) 934–942, doi:10.3139/146.101322.

[38] H. Schmid, E. Okunishi, W. Mader, Defect structures in ZnO studied by high-resolution structural and spectroscopic imaging, Ultramicroscopy 127 (2013) 76–84, doi:10.1016/j.ultramic.2012.07.014.

[39] S. Eichhorn, H. Schmid, W. Assenmacher, W. Mader, Homologous compounds of type $ARO_3(ZnO)_m$ in the system Ga-Sn-Zn-O, J. Solid State Chem. 246 (2017) 214–220, doi:10.1016/j.jssc.2016.11.031.

[40] J. Hoemke, E. Tochigi, T. Tohei, H. Yoshida, N. Shibata, Y. Ikuhara, Y. Sakka, Inversion domain network stabilization and spinel phase suppression in ZnO, J. Am. Ceram. Soc. 101 (2018) 2616–2626, doi:10.1111/jace.15426.

[41] S. Li, H. Lei, Z. Wang, J. Chen, P. Ruterana, Energetic and electronic properties of (0001) inversion domain boundaries in ZnO, Phys. Status Solidi B 255 (4) (2018) 1700429 –6, doi:10.1002/pssb.201700429.

[42] D. Zagorac, J.C. Schön, J. Zagorac, M. Jansen, Prediction of structure candidates for zinc oxide as a function of pressure and investigation of their electronic properties, Phys. Rev. B 89 (2014) 075201, doi:10.1103/PhysRevB.89.075201.

[43] E.H. Kisi, M.M. Elcombe, u parameters for the wurtzite structure of ZnS and ZnO using powder neutron diffraction, Acta Cryst. C 45 (1989) 1867–1870, doi:10.1107/S0108270189004269.

[44] Y. Wu, J. Kang, F. Liu, Pressure induced wurtzite-to-zinc blende phase transition in ZnO at finite temperature, J. Mater. Res. 23 (12) (2008) 3347–3352, doi:10.1557/JMR.2008.0410.

[45] Y. Ding, Z.L. Wang, T. sun, J. Qui, Zinc-blende ZnO and its role in nucleating wurtzite tetrapods and twinned nanowires, Appl. Phys. Lett. 90 (2007) 153510, doi:10.1063/1.2722671.

[46] Y. Yan, G.M. Dalpian, M. Al-Jassim., S.-H. Wei, Energetics and electronic structure of stacking faults in ZnO, Phys. Rev. B 70 (2004) 193206, doi:10.1103/PhysRevB.70.193206.

[47] I. Kubo, N. Tomiyama, Polarity of ZnO crystal (III) inversion twin boundaries on {101-0}, Jpn. J. Appl. Phys. 10 (1971) 952, doi:10.1143/JJAP.10.952.

[48] N. Shibata, H. Iwanaga, Inversion twin in zinc oxide crystal, Jpn. J. Appl. Phys. 11 (1971) 775–779, doi:10.1143/JJAP.11.775.

[49] J. Barf, T. Walther, W. Mader, Twin boundaries in zinc oxide with additions of gallium oxide, Interface Sci. 12 (2004) 213–226, doi:10.1023/B:INTS.0000028651.74657.2b.

[50] M. Bitenc, G. Dražić, Z. Crnjak Orel, Characterization of crystalline zinc oxide in the form of hexagonal bipods, Cryst. Growth Des. 10 (2010) 830–837, doi:10.1021/cg901193g.

[51] N. Daneu, A. Rečnik, S. Bernik, D. Kolar, Microstructural development in SnO_2–doped ZnO–Bi_2O_3 ceramics, J. Am. Ceram. Soc. 83 (2000) 3165–3171, doi:10.1111/j.1151-2916.2000.tb01699.x.

[52] D. Makovec, M. Trontelj, Extended defects in ZnO ceramics containing $Bi_4Ti_3O_{12}$ additive, J. Am. Ceram. Soc. 77 (1994) 1202–1208, doi:10.1111/j.1151-2916.1994.tb05393.x.

[53] N. Daneu, N. Novak Gramc, A. Rečnik, M. Maček Kržmanc, S. Bernik, Shock-sintering of low-voltage ZnO-based varistor ceramics with $Bi_4Ti_3O_{12}$ additions, J. Eur. Ceram. Soc. 33 (2013) 335–344, doi:10.1016/j.jeurceramsoc.2012.08.023.

[54] J.P. Perdew, K. Burke, M. Ernzerhof, Generalized gradient approximation made simple, Phys. Rev. Lett. 77 (1996) 3865–3868, doi:10.1103/PhysRevLett.77.3865.

[55] P. Giannozzi, S. Baroni, N. Bonini, M. Calandra, R. Car, C. Cavazzoni, D. Ceresoli, G.L. Chiarotti, M. Cococcioni, I. Dabo, A.D. Corso, S. de Gironcoli, S. Fabris, G. Fratesi, R. Gebauer, U. Gerstmann, C. Gougoussis, A. Kokalj, M. Lazzeri, L. Martin-Samos, N. Marzari, F. Mauri, R. Mazzarello, S. Paolini, A. Pasquarello, L. Paulatto, C. Sbraccia, S. Scandolo, G. Sclauzero, A.P. Seitsonen, A. Smogunov, P. Umari, R.M. Wentzcovitch, Quantum ESPRESSO: a modular and open-source software project for quantum simulations of materials, J. Phys.: Condens. Matter 21 (39) (2009) 395502–395519, doi:10.1088/0953-8984/21/39/395502.

[56] D. Vanderbilt, Soft self-consistent pseudopotentials in a generalized eigenvalue formalism, Phys. Rev. B 41 (1990) 7892–7895, doi:10.1103/PhysRevB.41.7892.

[57] A.M. Rappe, K.M. Rabe, E. Kaxiras, J.D. Joannopoulos, Optimised pseudopotential, Phys. Rev. B,**41** (1990) 1227, Erratum Phys. Rev. B44 (1991) 13175–13176, doi:10.1103/PhysRevB.44.13175.3.

[58] L. Franklin, C.E. Ekuma, G.L. Zhao, D. Bagayoko, Density functional theory description of electronic properties of wurtzite zinc oxide, J. Phys. Chem. Sol. 74 (2013) 729–736, doi:10.1016/j.jpcs.2013.01.013.

[59] D.C. Palmer, Visualization and analysis of crystal structures using CrystalMaker software, Z. Kristallogr. 230 (9–10) (2015) 559–572, doi:10.1515/zkri-2015-1869.

[60] P.A. Stadelmann, EMS – a software package for electron diffraction analysis and HREM image simulation in materials science, Ultramicroscopy 21 (2) (1987) 131–145, doi:10.1016/0304-3991(87)90080-5.

[61] Y. Kauffmann, A. Rečnik, W.D. Kaplan, The accuracy of quantitative image matching for HRTEM applications, Mater. Charact. 54 (2005) 194–205, doi:10.1016/j.matchar.2004.11.012.

[62] S. Labat, M.-I. Richard, M. Dupraz, M. Gailhanou, G. Beutier, M. Verdier, F. Mastropietro, T.W. Cornelius, T.U. Schülli, J. Eymery, O. Thomas, Inversion domain boundaries in GaN wires revealed by coherent Bragg imaging, ACS Nano 9 (9) (2015) 9210–9216, doi:10.1021/acsnano.5b03857.

[63] F. Lançon, L. Genovese, J. Eymery, Towards simulation at picometer-scale resolution: revisiting inversion domain boundaries in GaN, Phys. Rev. B 98 (2018) 165306, doi:10.1103/PhysRevB.98.165306.

[64] M. Žunić, Z. Branković, S. Bernik, M.S. Góes, G. Branković, ZnO varistors from intensively milled powders, J. Eur. Ceram. Soc. 27 (2007) 3897–3900, doi:10.1016/j.jeurceramsoc.2007.02.055.